

# Sco X-1: The Evolution and Nature of the Twin Compact Radio Lobes

E. B. Fomalont

*National Radio Astronomy Observatory, Charlottesville, VA 22903*

efomalon@nrao.edu

B. J. Geldzahler & C. F. Bradshaw

*School of Computational Sciences, George Mason University, Fairfax, VA 22030*

bgeldzahler@hotmail.com & cbradshaw@tstagg.com

## ABSTRACT

The motion and variability of the radio components in the low mass X-ray binary system Sco X-1 have been monitored with extensive VLBI imaging at 1.7 and 5.0 GHz over four years, including a 56-hour continuous VLBI observation in 1999 June. We detect one strong and one weak compact radio component, moving in opposite directions from the radio core. Their relative motion and flux densities are consistent with relativistic effects, from which we derive an average component speed of  $v/c=0.45\pm 0.03$  at an angle of  $44^\circ\pm 6^\circ$  to the line of sight. This inclination of the binary orbit suggests a mass of the secondary star that is  $< 0.9 M_\odot$ , assuming a neutron star mass of  $1.4M_\odot$ . We suggest that the two moving radio components consist of ultra-relativistic plasma that is produced at a working surface where the energy in dual-opposing beams disrupt. The radio lobe advance velocity is constant over many hours, but differs among lobe-pairs: 0.32c, 0.46c, 0.48c, and 0.57c. A lobe-pair lifetime is less than two days, with a new pair formed near the core within a day. The lobe flux has flux density that is variable over a time-scale of one hour, a measured minimum size of 1 mas ( $4 \times 10^8$  km), and is extended perpendicular to its motion. This time-scale and size are consistent with an electron radiative lifetime of  $< 1$  hr. Such a short lifetime can be caused by synchrotron losses if the lobe magnetic field is 300 G or by adiabatic expansion of the electrons as soon as they are produced at the working surface. The lobes also show periods of slow expansion and a steepening radio spectrum. Two of the core flares are correlated with the lobe flares under the assumption that the flares are produced by a coherent energy burst traveling down the beams with a speed  $> 0.95c$ .

The radio morphology for Sco X-1 differs from most other Galactic jet sources. Possible reasons for the morphology difference are: Sco X-1 is associated with a neutron star, it is a persistent X-ray source, the source is viewed significantly away from the angle of motion. However, the lobes in Sco X-1 are similar to the hot-spots found in many extragalactic radio double sources. Scaling the phenomena observed in Sco X-1 to extragalactic sources implies radio source hot-spot variability time-scales of  $10^4$  yr and hot-spot lifetimes of  $10^5$  yr.

*Subject headings:* binaries:close; galaxies: jets; radiocontinuum:stars; stars:neutron; stars:individual(Sco X-1); X-rays:stars

## 1. Introduction

Since Sco X-1 was first detected at radio frequencies in 1969 (Ables 1969), many observations at radio, optical and X-ray frequencies have been made in order to understand the physical processes associated with this object. It is identified with a 13-mag binary system with an orbital period of 0.787d (Gottlieb et al. 1975). The degenerate object is probably a neutron star, and the companion is an unknown spectral type with about a solar mass (Cowley & Crampton 1975). Sco X-1 is one of the most intense persistent X-ray sources and one of about 30 presently known low-mass X-ray binary (LMXB) systems. It is a ‘Z-type’ LMXB, named for a characteristic shape of its X-ray color-color diagram. It also exhibits quasi-periodic X-ray oscillations (QPO) from a few Hertz to kilo-Hertz (Hasinger & van der Klis 1989; van der Klis et al. 1996).

Radio observations in 1970 detected two symmetrical radio sources about one arcmin from Sco X-1 (Hjellming & Wade 1971). They were thought to be radio lobes of Sco X-1, but were later shown to be stationary extragalactic background objects having no relationship to Sco X-1 which has a significant measured proper motion (Fomalont & Geldzahler 1991). The results from a multiwavelength campaign (Hjellming et al. 1990) also suggested that there was only weak correlation of the radio emission with the optical and X-ray emission.

High-resolution radio observations at 5.0 GHz with the Very Long Baseline Array (VLBA) were initiated in 1995 in order to determine the trigonometric parallax of Sco X-1. From eight VLBA observations through 1998 August, a distance of  $2.8 \pm 0.3$  kpc was determined (Bradshaw et al. 1999). This distance (previous estimates ranged from 200 pc to 2000 pc (Westphal et al. 1968)) established that the X-ray luminosity was near the Eddington limit as inferred from X-ray models of Sco X-1 and other z-type LMXB’s (Lamb 1989; Penninx 1989; Vrtilik et al. 1991). The radio emission during these VLBA observations showed variability in intensity and structure over periods less than one hour, with discrete components moving away from the core at relativistic velocities.

With such variable radio emission in Sco X-

1, this source was established as another example of a Galactic-jet variable radio source (Mirabel & Rodriguez 1999) with strong similarities to the jet and lobe phenomena associated with luminous radio galaxies and quasars (Blandford & Rees 1974). The evolutionary time scales associated with accretion disks and jets scale roughly with the luminosity and mass of the degenerate object. Thus, significant changes should occur over hours and days in the evolution of Galactic sources that would take millions of years in quasars.

Experience gained from the eight VLBA observations used to determine the parallax of Sco X-1 showed that the four to six hour observations made every six months were not sufficient to determine a coherent story for the radio emission from Sco X-1. Each observation was too short to follow much of a component’s evolution, and the individual observations were too separated in time to follow the evolution. For this reason, we observed Sco X-1 with VLBI resolution for a continuous 56-hour period in 1999 June. The results from this series of observations were crucial to understanding the radio evolution of Sco X-1 and formed a framework for understanding the previous VLBA observations.

We have already reported results associated with some of these data. The parallax was given by (Bradshaw et al. 1999), and Paper I (Fomalont et al. 2001) discussed the kinematic properties of the radio source; the space motion of the lobes and the speed of the energy flux in the beam. This paper is organized as follows. The nine VLBI observations, and the data reduction methods are described in §2. Because we display VLBI snapshots (images made from observations less than about two hours), the difficulties and ambiguities with such imaging are described. The images in §3 from the 1999 June 11-13, 56-hour VLBI observation and the 1998 February 27-28, observations are presented and discussed. Then, images from the other less extensive observations are shown and compared with the more extensive observations. In §4 we review the kinematic properties of Sco X-1 (Paper I) and estimate the stellar component masses of Sco X-1 from the orbital inclination. The detailed physical properties and suggested production mechanisms associated with the lobes are discussed in §5. The optical, X-ray

and radio properties and evolution of the core will be discussed elsewhere (Geldzahler et al. 2002). The comparison with extragalactic radio sources is given in §6, and our conclusions are summarized in §7.

## 2. Observations and Data Processing

Table 1 contains the log of all VLBI observations of Sco X-1. The first eight observations with the VLBA, between 1995 August and 1998 August, were planned to optimize the determination of the trigonometric parallax. The 56-hour monitoring of Sco X-1 in 1999 June was composed of a series of seven consecutive eight-hour observations amongst three different VLBI arrays: VLBA+VLA (the Very Large Array), the APT (Asia-Pacific Telescope), and the EVN (European VLBI Network + additional telescopes). Extensive optical and X-ray observations were also made during this period (Titarchuk et al. 2001; Bradshaw et al. 2002; Geldzahler et al. 2002).

### 2.1. Observations and Data Correlation

The VLBA observations alternated between Sco X-1 for 9 minutes and the calibrator (1504-166) for 2 minutes. Three pairs of observations were made at 5.0 GHz followed by one pair at 1.7 GHz. The APT and EVN observations were made solely at 5.0 GHz and the observing schedule alternated between Sco X-1 for 19 minutes and the calibrator source for 3 minutes. The VLBA and EVN observations were observed with a total bandwidth of 128 MHz with one-bit sampling, whereas the APT observations used a total bandwidth of 32 MHz, but with two-bit sampling. The VLA was used in two ways: as one element of the VLBA and as a stand-alone array from which arc-second resolution images were obtained for Sco X-1 (Geldzahler et al. 1983; Bradshaw et al. 1997).

A background radio source, about  $70''$  NE of Sco X-1, has a correlated flux density of 8 mJy at 5.0 GHz and 14 mJy at 1.7 GHz. This object is the north-eastern of the two sources near Sco X-1 which were previously thought to be related to the binary system (Fomalont & Geldzahler 1991). This source is sufficiently strong and compact to be used as the primary phase calibrator for Sco X-1 (Bradshaw et al. 1999) at both frequencies. We will designate this radio source as the North-East

in-beam calibrator (NEIBC). Because the effective primary beam of the phased arrays (VLA, Westerbork and ATCA) were smaller than the  $70''$  separation between Sco X-1 and the NEIBC, these arrays alternated observations between Sco X-1 and the NEIBC with three-minute cycles. All other telescopes pointed midway between the two sources and observed them simultaneously.

The VLBA and EVN data were processed by the VLBA correlator in Socorro, NM, USA. The data from the APT observations were processed with the S2-correlator in Penticton, BC, Canada. All data associated with the observations of Sco X-1 were correlated at two positions: (1) Sco X-1 at  $\alpha = 16^{\text{h}}19^{\text{m}}55.085^{\text{s}}$ ,  $\delta = -15^{\circ}38'24.90''$ ; (2) NEIBC at  $\alpha = 16^{\text{h}}19^{\text{m}}57.439^{\text{s}}$ ,  $\delta = -15^{\circ}37'24.0''$  (epoch J2000).

### 2.2. Calibration

The observations of 1504-166 were used to determine the delay offset and delay rate for each antenna, predominantly caused by the differences in the independent clocks and oscillators, and to check the general quality of the data. The delay and delay rates were determined by using routine FRING in the AIPS software package (Greisen 1988). The total flux density of the calibrator was measured to 2% accuracy using the VLA observations of 3C286 to determine the absolute flux density scale of the observations. The milliarcsecond structure of 1504-166 was determined from the VLBA observations, and this model was used to determine the gain calibration for all of the data, with an accuracy of about 3%.

The data for the VLBA and EVN observations consisted of 8 independent streams, at 4 contiguous frequencies each with 2 polarizations, and the APT observations contained 2 data streams. After the 1504-166 calibrations, all data streams were combined to increase the signal-to-noise ratio (SNR) for the next calibration step using the relatively weak NEIBC. With the AIPS routine CALIB, we determined the residual phase error for each antenna every few minutes from the observations correlated at the NEIBC position. At 1.7 GHz, its correlated flux density was  $> 10$  mJy on the longest VLBA baseline; hence, an accurate antenna phase error could be determined from two minutes of data. This time is shorter

than the time-scale of phase changes except during rare periods of ionospheric turbulence. When the phase could not be connected unambiguously between consecutive phase solutions, the data between these two times were omitted from the analysis.

At 5.0 GHz the calibration strategy was more complicated. The NEIBC correlated flux density decreased from 8 mJy at the shorter baselines to 3 mJy for the longer baselines. At least two minutes (five minutes for the APT baselines) integration was needed to determine phase errors for these baselines. For low elevation observations or during periods of poor phase stability, phase solutions were ambiguous. Hence, at 5.0 GHz the NEIBC could reliably calibrate baselines shorter than 3000 km. After this initial calibration of the shorter baselines, further self-calibration of Sco X-1 successfully reinstated the longer baselines when Sco X-1 was stronger than about 5 mJy.

With the simultaneous observations of the small-diameter NEIBC, the calibration of Sco X-1 allowed us to register all images over the four-year period on the same astrometric grid with an estimated accuracy of  $< 0.1$  mas (Bradshaw et al. 1999). The image registration of Sco X-1 was not altered when the data were further self-calibrated in order to add the longer spacings. This registration assumed that the NEIBC was stationary with the same centroid at the two frequencies. This assumption is reasonable because: (1) The source had not varied at either frequency over the last 15 years of VLA monitoring, (2) its structure is symmetric, with an angular size of 2.5 mas at 5.0 GHz and 3.5 mas at 1.7 GHz, and (3) its spectral index is  $-0.4$  ( $S \propto \nu^\alpha$ ), suggesting the lack of a significant small-diameter opaque component, which might be variable. The source was not identified to a magnitude limit of  $25^m$  (Malin, priv comm, cited in (Geldzahler et al. 1981)).

### 2.3. Imaging, Self-Consistency and Parameterization

Deconvolved images of Sco X-1 were made using the routine IMAGR in AIPS and with the Caltech software package Difmap (Shepherd 1997). Images of the NEIBC were also made as a check on the quality of the calibration. Due to significant variability of Sco X-1 during the observations, image artifacts associated with the aperture

synthesis of variable sources often affected an image made from more than one hour of data. For the VLBA observations, when the SNR was sufficient (the flux density was more than about 5 mJy), images could be made every hour at 1.7 GHz from one 9-minute observation and at 5.0 GHz from three 9-minute observations. If Sco X-1 was weaker than 5 mJy, longer periods of data were combined in order to obtain images with a useful SNR.

The u-v coverage in the hour-to-hour VLBA snapshots was sparse, especially during the first and last hour of an observation, when the coverage contained large gaps. An rms noise of 0.2 mJy/beam for each snapshot, a peak intensity in the range 1.5 and 20 mJy/beam, and a somewhat noisy phase calibration using the relatively weak NEIBC, when combined with the relatively poor u-v coverage and the source variability, conspired to make the determination of reliable radio images ambiguous. For some snapshots, an unrestrained deconvolution of the images produced physically unacceptable image characteristics which often had properties of the dirty beam which varied through the observation day. However, the relatively simple structure of Sco X-1 (a few bright small-diameter components along a well-defined position angle) made the deconvolution less ambiguous than with a more complicated source. The justification of this assumption is that the use of this simple model (which means that only a small region of the image was searched for emission using the deconvolution algorithms) led to consistent results for the entire body of data.

Two methods were used to judge the quality of the deconvolution of the images of Sco X-1. First, reasonable continuity of the images between consecutive epochs was expected. Sudden changes in the source structure or image features which resembled the ‘dirty-beam’ suggested a poor deconvolution or bad data quality. The data were then scrutinized, the NEIBC calibration stability was checked, the source reimaged, and deconvolved. Secondly, the hourly data sets were also processed by the Difmap processing package. By fitting simple Gaussian component models directly to the visibility data, some of the ambiguities of image-plane deconvolution were avoided. If the Difmap model did not agree well with the image, further checking was necessary. Finally,

the independent images made at 5.0 GHz and 1.7 GHz had to be consistent; that is, the components at the two frequencies were nearly coincident, although the 1.7 GHz lower resolution observations did occasionally show more extended emission, as expected on physical grounds. The difference in angular scale between the 1.7 and 5.0 GHz beam properties by a factor three also aided in determining real structure from beam-induced artifacts. Simulations were also made in order to quantify the reliability and proscribe the proper reduction methods. Data errors associated only with the expected level of stochastic receiver noise should cause little ambiguity in the images. Other potential data errors (unknown data drop-outs, strong source variations, rapid atmospheric phase variations over minute time-scales) were modeled, showing that relatively large errors could lead to significant image errors. For this reason we removed marginal data, especially for the longer baselines where these non-random errors occurred, with the concomitant loss of resolution for some snap-shots.

For the 5.0 GHz EVN and APT observations, a similar imaging and reduction strategy was used. The NEIBC was only useful in calibrating the European baselines in the EVN and the Australian baselines for the APT. If Sco X-1 was sufficiently strong ( $> 5$  mJy for the EVN,  $> 10$  mJy for the APT), then the other antennas could be self-calibrated using Sco X-1. However, the u-v coverage for these arrays was significantly worse than that for the VLBA, so the data had to be averaged over several hours before reliable snapshot images could be made. For the APT observations, two images separated by about three hours were made. For the EVN observation, three images, separated by about two hours, were made.

The resolution of an image depended on the SNR and the elevation of the source. For VLBA observations at 1.7 GHz, all images were convolved to a full-width half-power resolution of  $10 \times 5$  mas at position angle  $0^\circ$ , although the resolution of the observations varied somewhat during the day. At 5.0 GHz, imaging using only the shorter spacings, produced the same resolution as that at 1.7 GHz. These image pairs were used to determine the spectral index distribution across Sco X-1. At 5.0 GHz, when the source was frequently stronger than 5 mJy and self-calibration of the

longer baselines was possible, the resolution was about  $4.5 \times 1.5$  mas during the middle part of the day. The resolution degraded to  $6 \times 2$  mas at low elevation angles. For the occasional periods when Sco X-1 was stronger than about 15 mJy, a resolution of  $3 \times 1$  mas was obtained.

The flux density, position and angular size for the discrete radio components in Sco X-1 were determined in two ways: (1) fitting Gaussian-components directly to the image, and (2) fitting Gaussian-components to the visibility data. Although errors were estimated from each of the two methods, the difference in the radio source parameters from the two analysis were used as a better accurate estimate of the real uncertainties.

### 3. The Radio Images of Sco X-1

#### 3.1. 1999 June 11-13; MJD 51340-51342

##### 3.1.1. *The Images and Component Parameters*

Figure 1 shows the changing structure of Sco X-1 with  $10 \times 5$  mas resolution at 1.7 GHz and 5.0 GHz from the VLBA observations. These images, although only covering 40% of the observation, form a consistent set from which general evolution properties are evident. The vertical dashed line shows the position of the binary system, as determined from its radio parallax (Bradshaw et al. 1999). The skew dashed-line to the left shows the location of the component northeast of the core as a function of time. On MJD 51342, the vertical line to the right shows the approximate position of the component southwest of the core. The locations of the dashed lines on the 1.7 GHz and 5.0 GHz columns are identical.

More details of the changing structure of Sco X-1 are shown in Figure 2. These 5.0-GHz images are at the highest resolution obtained during the 56-hour experiment. The image snapshots are separated by about 50 minutes for the VLBA observations and about 2.5 hours for the APT and EVN observations. The APT and EVN images have a resolution of  $10 \times 5$  mas, and most of the VLBA images have a resolution of  $4.5 \times 1.5$  in position angle  $0^\circ$ . The image field of view is  $35 \times 25$  mas for MJD 51340 and 51341 and  $90 \times 25$  mas on MJD 51342. The vertical lines follow the same tracks as in Figure 1.

Two estimates of the total flux density for Sco

X-1 are shown in the top two plots of Figure 3. The flux density, shown in Figure 3a, was determined from the VLA observations with determination of the flux density made every 10 minutes. With a resolution of  $3''$  at 5.0 GHz and  $10''$  at 1.7 GHz, these measurements contain the entire emission from Sco X-1. Figure 3b shows the total flux density obtained from the VLBA images. The good agreement between the VLA and the VLBA measurements indicates that no significant large-scale structure associated with Sco X-1 was resolved out by the VLBA observations. Figures 3c, 3d and 3e show the flux density for each of the three components. In Figure 4, the spectral index  $\alpha$  of each of the three components during the dual-frequency VLBA observations is shown.

### 3.1.2. A Description of the Changes in Sco X-1

The 1999 June observations form a basis for the interpretation of the radio emission from Sco X-1. Thus, we will describe the evolution seen in the images in some detail.

The basic morphology of Sco X-1 is simple. The source is usually composed of three relatively compact components: a radio core that is nearly coincident with the binary system, a compact NE component moving away from the core; a weak SW component moving away on the opposite side of the core. The three components lie along an axis of position angle  $54^\circ$  to an accuracy of a few degrees.

Changes associated with the emission from Sco X-1 are as follows:

- **MJD 51340.1 to 51340.4.** The NE component reached a maximum intensity, with  $\alpha = -0.5$ , at MJD 51340.2. Subsequently, it faded, became more extended with a steepening spectral index, and fell below the VLBA detection level at MJD 51340.4. It did not reappear over the next ten hours in the images from the APT and EVN. During this period, the radio core flux density steadily increased with  $\alpha > 0.0$ .
- **MJD 51340.4 to 51341.3.** The radio core decreased in flux density from 20 mJy to 8 mJy in a few hours (the rms error for a flux density measurement is about 0.5 mJy.) No emission to the north-east was present. At

MJD 51340.7 the core flux density began to increase, and by MJD 51341.0, the flux density had reached 20 mJy. The images clearly show that this rise in flux density was associated with a component emerging from the core to the northeast. Between MJD 51341.0 to 51341.3, this new NE lobe moved outward and decreased in flux density. Emission between the lobe and core was also present. The core flux density generally decreased in flux density during this period, but a small flare occurred at MJD 51341.3.

- **MJD 51341.3 to 51341.8.** After moving about 20 mas from the core, the NE component brightened, slowly at first, and then abruptly flared from 2.8 mJy to 20 mJy in less than one hour. The spectrum quickly flattened to  $\alpha = -0.5$ , then NE flux density slowly decayed to 1.5 mJy over the next 15 hours and its spectral index dropping to  $\alpha \approx -1.2$ . The radio core, during this period, remained relatively constant at 4 mJy, except for a flare to 8 mJy at MJD 51342.3
- **MJD 51341.8 to 51342.2.** The radio core brightened from 4 mJy to 20 mJy, reaching the peak at MJD 51342.0. The radio core then decreased in flux density and by MJD 51342.1 extended emission towards the northeast was clearly present. However, unlike the core flare and subsequent expulsion of emission to the NE about 1.3 days earlier, this extended emission decreased below the detection level by MJD 51342.2 and with no apparent motion. The SW component, seen better in the lower resolution 1.7 GHz images, is visible during this period. The NE component decreased slowly in flux density.
- **MJD 51342.2 to 51342.4.** For the last four hours of the observation, the NE component brightened from 1.5 to 4 mJy and the spectral index flattened again to  $-0.5$ . This NE component flare is less spectacular than the one about 0.8 days earlier, but has similar properties. The core remained steady at about 4 mJy with no resolvable extended structure.

### 3.2. 1998 February 27-28; MJD 50871-2

The only previous Sco X-1 observation on consecutive days occurred on 1998 February 27-28, from two six-hour VLBA observations separated by 18 hours. The upper part of Figure 5 shows three sets of snapshots, each 52 minutes apart on MJD 50871. The lower two panes show the structure on the following day when the source was weaker. Figure 6 shows the flux density of the three components on both days. Although there was some indication of extended structure between the core and the NE component, the high-resolution 5.0 GHz images show that most of the emission was contained in compact components.

On February 27, the core spectrum was inverted with flux density about 10 mJy at 5.0 GHz. The NE component had a flux density  $> 15$  mJy and was moving from the core in the same position angle as that in the 1999 June observations. Near the end of the observation period the flux density decreased, its spectral index became steeper and the angular size increased. This behavior will be discussed in more detail in §5.7 and with Figure 14.

Sco X-1 was much fainter on the following day and individual snapshots were too noisy to show rapid changes. At the bottom of Figure 5, the 1.7 GHz and 5.0 GHz images, both with  $10 \times 5$  mas resolution, were made from the entire 5-hour observation. The core was unresolved with a peak flux density of 3.0 mJy, and decreased during the day. The SW component, clearly detected at about 2 mJy, was also relatively compact. The radio emission northeast of the core was complex but confined along the major axis of the radio structure, between 30 mas to 60 mas from the core at 1.7 GHz. In the 5.0 GHz image, only two features in this northeast emission region were detected above the noise level. A linear extrapolation of the NE component motion on MJD 50871 intercepts the most distant component of emission in the northeast direction on MJD 50872. Motion of the SW component was detected on both two days, and is discussed in the following section.

### 3.3. The Component Velocities and Orientations

The 1998 February and 1999 June images show the major dynamical properties of Sco X-1. A

compact component was always present near the binary system. It varied significantly in flux density and occasionally faint emission extended several mas towards the north-east. A compact component was usually detected northeast of the radio core and its motion was clearly directed away from the radio core. Its flux density also varied significantly over hour time scales. A compact component southwest of the core was detected about 50% of the time and was on average about 10 times weaker than the NE component.

The relative simplicity of these images of Sco X-1 is contrasted by the more complicated emission from other well-studied Galactic-jet radio sources (Mirabel & Rodriguez 1999). Although their structures tend to lie on a well-defined axis, they are often composed of many components on both sides of the radio core. For Sco X-1, we find that *only one compact component was detected on the NE and SW sides of the radio core* (See Figure 11 for a possible exception).

The changing separation of the NE and SW components from the core for the 1999 June (top) and 1998 February (bottom) observations is shown in Figure 7. For the 1999 June observations, the velocity in the plane of the sky for the NE component #1, detected for 6 hours on MJD 51340, was  $v = 0.73 \pm 0.07$  mas hr<sup>-1</sup> = 0.28c<sup>1</sup>. The NE component #2 was not resolved from the core until about MJD 51341.0. Then, from MJD 51341.0 to 51341.35, the NE component speed was  $v = 1.74 \pm 0.16$  mas hr<sup>-1</sup> = 0.68c. After MJD 51341.4, when the NE component flared, the component speed decreased to  $v = 1.25 \pm 0.05$  mas hr<sup>-1</sup> = 0.49c. Although the NE component varied considerably in flux density during the last 24 hours of the observations, its speed remained nearly constant.

For the 1998 February observations, the velocity of the NE component on MJD 50871 was  $v = 1.11 \pm 0.06$  mas hr<sup>-1</sup> = 0.43c over the five hours of observations, with no significant departure from linearity except for the last frame. The single point for the NE component on MJD 50872 was taken as the position of the most distant part of the NE component seen in Figure 5.

Motion of the SW components was more dif-

---

<sup>1</sup>For a measured distance to Sco X-1 of 2.8 kpc, one mas = 2.8 AU =  $4.19 \times 10^{13}$  cm. A speed of 1 mas hr<sup>-1</sup> = 0.388c.

difficult to detect. On MJD 50872 the component was both strong and long lasting and moving away from the core with  $v = 0.6 \pm 0.2 \text{ mas hr}^{-1}$ . On MJD 51342 the velocity was  $v = 0.5 \pm 0.3 \text{ mas hr}^{-1}$ . In Figure 7, the dashed-lines passing through the positions of the SW components are not linear fits to its position, but to **50% of the fitted angular separation to the NE component** (Figure 12 shows a plot of this ratio from all Sco X-1 observations). Thus, we surmise that the SW component was also moving away from the core, but at a projected velocity of about 50% of that of the NE component. These motions are described in more detail in §4.1.

The orientation of the NE and SW components with respect to the core for the 1999 June and 1998 February observations are shown in Figures 8a and 8b. The radio structure of Sco X-1 remained near position angle  $54^\circ$  during these two observations, and the component orientations from the previous observations of Sco X-1 also lie within a few degrees of  $54^\circ$ . Hence, any long-term variation in the orientation of the radio emission from Sco X-1 is less than about three degrees. It is possible to fit the position angle distribution in 1999 June observations with a mean value of  $54^\circ$  plus a sinusoidal term of  $\approx 3^\circ$  with a period of between two to four days. Modeling of the binary system X-ray QPO's suggest that the neutron star/accretion disk interaction could produce a  $5^\circ$  precession over several days (Titarchuk & Osheroich 2000).

### 3.4. The 1995-1996 VLBA Observations at 5.0 GHz

The first four VLBA observations of Sco X-1 were made on 1995 August 19 (MJD 49948), 1996 March 16 (MJD 50158), 1996 September 16 (MJD 50340) and 1996 August 3 (MJD 50663), and contour plots of the radio emission are shown in Figure 9. These observations had lower sensitivity than later observations, were only at 5 GHz, and were about four hours in duration. The radio emission from Sco X-1 during these observations was relatively weak so that images made from one-hour slices of the data were too noisy in order to determine variability and motion. Nevertheless, all four observations showed similar properties in the emission of Sco X-1.

- **MJD 49948.** The radio core had a peak flux density of 0.32 mJy. There was a trace of both the NE component and the SW component 19 mas and 12.2 mas from the core respectively, each with a peak flux density of  $< 0.20 \text{ mJy}$ .
- **MJD 50158.** The radio core had a peak flux density of 0.50 mJy. There was a slight indication of the NE component 14 mas from the core, with a peak flux density  $< 0.25 \text{ mJy}$ .
- **MJD 50340.** The source was stronger during this observation and all three components were present well above the noise. The SW component had an integrated flux density of 2.5 mJy, located 5 mas from the core. The core flux density increased from 0.30 mJy to 0.60 mJy during the four-hour observations. The NE component was about 8 mas from the core with a peak flux density of about 0.6 mJy. The distance ratio of the NE and SW components from the core was about 2:1.
- **MJD 50663.** The core had a peak flux density of 2.0 mJy and the NE component was detected, about 26 mas away, with a peak flux density of 0.35 mJy. Any SW component was  $< 0.15 \text{ mJy}$ .

The relative weakness of Sco X-1 in 1995-1996, compared with later observations, is consistent with the general characteristics of the long-term flux density behavior of Sco X-1, as shown from the Green Bank Interferometer monitoring between MJD 50600 and 51700 (see [www.gb.nrao.edu/fgdocs/gbi/pubgbi/ScoX-1](http://www.gb.nrao.edu/fgdocs/gbi/pubgbi/ScoX-1)). At the monitoring frequency of 8 GHz, the quiescent level of Sco X-1 remained at 5 mJy for a period of 100 to 150 days, but there were periods of enhanced emission at 10 to 15 mJy which persisted for 50 to 100 days. About 5% of the time there were large outbursts ( $> 50 \text{ mJy}$ ), which lasted over a few days. These outburst occurred randomly and were not associated with the periods of enhanced emission from Sco X-1.

### 3.5. 1998 August 29-30, MJD 51054-5

Figure 10 displays the structure of Sco X-1 for a five-hour observation on August 29-30, 1998. Be-



cause of the weakness of the source, each image contains data from the entire five-hour observation. All three components were present, although the core was barely detectable at either frequency. The NE component was clearly extended and contained several emission peaks along the source major axis. The SW component was compact and relatively strong. The appearance of Sco X-1 on this day was similar to that on MJD 50872, shown at the bottom of Figure 5. However, the linear size of the source on MJD 51054 was a factor of three smaller. Again, the ratio of the separation from the core of the NE and SW components was about 2:1.

### 3.6. 1997 August 22, MJD 50682

During this five hour VLBA observation, Sco X-1 was extremely bright and nearly all of the emission was contained within 5 mas of the core, as shown in Figure 11. The high-resolution image showed emission moving outward from the binary system, particularly on the north-east side of the core. The relatively bright spot of emission at the extreme edge of the extended emission was advancing at a velocity of  $1.4 \pm 0.3 \text{ mas h}^{-1}$ . Some emission was also detected SW of the core. This morphology and evolution was similar to that seen on MJD 51341.0 when the second NE component was ejected from the core. The spectral index of the emission within 5 mas of the core rose from  $\alpha = 0$  to  $\alpha = 0.3$  during the five hour observation.

A faint component, about 20 mas NE of the core, was also detected. This is the only example of two radio components on one side of the core. However, the distant component is extremely weak with no measured motion. The radio structure on this day will be discussed in more detail elsewhere (Geldzahler et al. 2002).

## 4. Orientation of the Binary system

### 4.1. Doppler-Beaming of NE and SW Components

The kinematic results discussed in the section, have already been reported in Paper I. We present more detail in this section.

The images from the 1998 February and 1999 June observations showed that there was often a compact NE component moving away from the

core. Although this component varied significantly in flux density, its velocity remained relatively constant over periods of many hours. When the NE component was well-separated from the core, its measured speeds *in the plane of the sky* were 0.28c, 0.43c, 0.49c and 0.68c. On MJD 51341 and MJD 50682 a NE component emerged from the core. Because of a lack of sufficient resolution, the emergent velocity was not well-defined, although it was about 0.5c.

Motion of the SW component away from the core was observed during the 1998 February and 1999 June observations, with  $v = 0.6 \pm 0.2 \text{ mas hr}^{-1}$ , and  $v = 0.5 \pm 0.3 \text{ mas hr}^{-1}$ , respectively. Further detection of the motion was not possible because of the weakness and intermittent detection of this component. A comparison of the NE-to-core and the SW-to-core component distance ratio of all the observations is shown in Figure 12. There is no systematic variation with distance and the average ratio is  $0.51 \pm 0.02$ . Since the NE component was moving away from the core, we infer that the SW component was also moving away from the core in the opposite direction with 51% of the velocity of the NE component.

Another comparison of the radiative properties of the NE and SW components is given in Figure 13, which displays the spectral index versus flux density for the two components in Sco X-1 from all of the observations whenever it was determined. For comparison, the spectral properties for the core are shown (Geldzahler et al. 2002). When the flux density of the NE component was stronger than 4 mJy its spectral index was  $\alpha \approx -0.6$  but decreases to  $< -0.9$  at fainter flux densities. The SW component was detected less than 50% of the time and often only at 1.7 GHz. Its greatest flux density was 5 mJy at 1.7 GHz and the spectral index was about  $-0.6$ ; hence, the flux density at 5.0 GHz is about half of that at 1.7 GHz. We conclude that on average the apparent brightness of the SW component is about ten times fainter than that of the NE component. Furthermore, the spectral index of the SW component at its brightest was about equal to that of the NE component at its brightest. We will discuss the flux density ratio between the two lobes in more detail in §5.9

The relative positions and velocities of the NE and SW components, their relative flux density (in a statistical sense since both components vary con-

siderably), and their spectral properties suggest strongly that the NE and SW components have similar properties, with the observed emission differences resulting from relativistic aberration and Doppler beaming. The observed apparent motion in the plane of the sky of a component moving with a velocity  $v$  (usually given in term of  $c$  as  $\beta = v/c$ ), at an angle of  $\theta$  to the line of sight is (1):

$$\beta_{NE} = \frac{\beta \sin(\theta)}{1 - \beta \cos(\theta)} \quad (1)$$

$$\beta_{SW} = \frac{\beta \sin(\theta)}{1 + \beta \cos(\theta)} \quad (2)$$

where  $\beta_{NE}$  is the observed velocity in the plane of the sky of the component approaching the observer and  $\beta_{SW}$  is the velocity of the receding components.

We have measured a range of speeds for the NE component. However, the nearly constant position angle of the axis of Sco X-1 in the plane of the sky (Figure 8) strongly suggests that the direction of the space velocity of the lobes with respect to the line of sight is also constant. To determine an average speed of the two Sco X-1 components, we considered the time ranges MJD 51341.0 to 51342.4 and MJD 50871.3 to 50872.4. These periods are instances when the NE component speed was determined over a long period of time and the SW component was relatively strong. These two periods yield a measured proper motion of  $v = 1.25 \pm 0.05$  and  $v = 1.11 \pm 0.06$  mas hr<sup>-1</sup>. We will thus assume that the average speed of the NE component of Sco X-1 of  $1.18 \pm 0.08$  mas hr<sup>-1</sup>. At a distance of  $2.8 \pm 0.3$  kpc for Sco X-1, the average speed of the NE component in the plane of the sky is then  $\beta_{NE} = 0.46 \pm 0.08$ , with the distance uncertainty incorporated in the error. Next, we adopt the ratio of the SW speed to the NE speed as  $0.51 \pm 0.02$ . This ratio is a function of the speed, but should be the appropriate value that we have adopted. Equations (1) and (2) become:

$$\frac{\beta_{SW}}{\beta_{NE}} = 0.51 \pm 0.02 = \frac{1 - \beta \cos(\theta)}{1 + \beta \cos(\theta)}, \quad (3)$$

$$\beta_{NE} = 0.46 \pm 0.08 = \frac{\beta \sin(\theta)}{1 - \beta \cos(\theta)}, \quad (4)$$

from which we obtain

$$\beta = 0.45 \pm 0.03; \quad \theta = 44^\circ \pm 6^\circ. \quad (5)$$

The quoted errors are the one-sigma uncertainties and include the measurement errors.

The determination of the Doppler boosting associated with the flux densities of the NE and SW components requires a specific model of their internal structure, particle motion and magnetic field geometry as discussed in §5.5. If we assume that the moving components are transparent, with all particles moving at the bulk velocity and radiating isotropically, then the flux density ratio,  $R$  is given by (Blandford & Königl 1979; Cawthorne 1991):

$$R = \left[ \frac{\beta_{SW}}{\beta_{NE}} \right]^{k-\alpha} \quad (6)$$

where  $k$  is a geometric factor which equals 2 for an optically thin source, and  $\alpha$  is the spectral index of the source emission. From the measured  $\alpha = -0.6$  we obtain a predicted flux density ratio of  $R=0.17$ , which is somewhat larger than that observed (see §5.9 for more details). Thus, the space motion derived solely from the relative motions of the two components is in reasonable agreement, considering many uncertainties about the radiation properties and variability of the lobes.

## 4.2. Sco X-1 Binary Masses

Assuming that the radio beam lies along the rotation axis of the accretion disk which in turn lies in or close to the orbital plane of the binary system, we can better determine some of the properties of the binary. The relative constancy of the radio axis over five years are supports the above association.

The mass function for the Sco X-1 binary has been derived from the measured radial velocity of the HeII  $\lambda$ -4686 line, presumably from the accretion disk, and is given by  $F(M) = (M_2 \sin i)^3 / (M_1 + M_2)^2 = 0.016 \pm 0.004$  (our estimated error), where  $M_1$  and  $M_2$  are the masses of the neutron and secondary star, respectively, and  $i$  is the inclination of the orbit (Cowley & Crampton 1975). The binary is composed of a degenerate star, almost certainly a neutron star (Hasinger & van der Klis 1989). Measurements of many neutron star systems produced estimated masses between 1.2 to 1.6  $M_\odot$  (Lewin et al. 1995). The intrinsic X-ray luminosity of Sco X-1, for a distance of 2.8 kpc, also suggests a neutron star mass of about 1.4  $M_\odot$ .

The calculated secondary mass  $M_2$ , from the best value of the mass function, inclination and neutron star mass, is  $(0.63 \pm 0.26) M_\odot$ . Such a low companion mass is a problem for most models of the energetics in Sco X-1. First, the star may not fill its Roche lobe resulting in an accretion rate that is too low; perhaps the companion is an evolved star. Secondly, infra-red spectroscopic observations of the binary system suggest that the secondary star is earlier than G5 (Bandyopadhyay et al. 1999). However, the X-rays from Sco X-1 in all likelihood heat up the atmosphere of the secondary, puffing out its atmosphere until it overflows the Roche lobe resulting in mass accretion onto the compact star.

The secondary star mass estimates can be increased in the several ways. If the degenerate star mass is  $> 3.5 M_\odot$ , then the secondary star would have a mass  $> 1 M_\odot$ . But, then what is the nature of the degenerate star? A mass function  $> 0.025$  would also increase the secondary star mass associated with a  $1.4 M_\odot$  neutron star. This implies that the optical lines are coming from a much larger region than the accretion disk near the neutron star. Thus, the masses of the neutron star and the secondary member of the Sco X-1 binary are still uncertain even with knowledge of the orbit inclination.

## 5. The Nature of the NE Component

### 5.1. Angular and Linear Size

The angular size of the NE component could be measured with an accuracy of 0.5 mas when it had a flux density  $> 5$  mJy. Figure 14 shows a plot of the angular size and motion of the NE and core components for the seven snapshots on MJD 50871 (see Figure 5 also) when both the core and NE components were relatively strong. The angular sizes were determined by fitting the visibility data directly to an elliptical Gaussian model and by fitting the component brightness on the image and deconvolving the effects of the beam shape. Both methods gave consistent results.

The comparison of the positions and sizes of the core and the NE components provides a good indication of the robustness of these measurements. The core was about 10 mJy, relatively stationary and extended in the direction along the source major axis, as was commonly observed at other

epochs. Alternatively, the NE component was extended orthogonal to the direction of motion and was clearly moving away from the core. Since the effects of noise and poor phase calibration will blur all of the emission in the same way, the different size and orientation of the core and NE components strongly suggests that these measured angular sizes and orientations are valid.

For snapshots 1 through 3 in Figure 14, the measured average angular size and orientation of the NE component itself was  $(1.5 \pm 0.15) \times (0.9 \pm 0.2)$  mas in position angle (pa)  $140^\circ \pm 15^\circ$ . The angular size in snapshot 4 is marginally bigger and the size for snapshot 5 is  $2.4 \times 1.3$  mas in pa  $120^\circ$ . In the 50-minute separation between snapshot 5 and 6, the component increased in area by a factor of 4.5, to  $5.0 \times 2.9$  mas in pa  $150^\circ$ , an expansion at a velocity close to  $c$ . In snapshot 7 the size of the component did not increase substantially, but the bulk motion of the emission may have decreased. The angular size of the NE component was also accurately determined on MJD 51341.4 and MJD 51342.3. The angular sizes were  $(1.6 \pm 0.1) \times (0.7 \pm 0.3)$  mas in pa  $135^\circ \pm 10^\circ$  and  $(2.4 \pm 0.3) \times (0.8 \pm 0.4)$  mas in pa  $155^\circ \pm 30^\circ$ , respectively, in good agreement with the minimum size of the NE component on MJD 50871.

The NE component is clearly extended in the direction perpendicular to its motion. In addition, the measured size in this direction of motion is slightly increased by the component motion during each snapshot over a 33-minute span. During this period, the component moves 0.6 mas; hence, the measured size of 0.9 mas corresponds to a true size of about 0.7 mas after removing the blurring from the motion. Thus, we derive a minimum component size (full-width at half power) of  $1.5 \times 0.7$  mas, corresponding to  $6.3 \times 10^8$  km by  $2.9 \times 10^8$  km with the major axis perpendicular to the orientation of the source. More detailed measurement of the NE component structure, other than its angular size, cannot be obtained with the present resolution and SNR.

The flux densities and spectral indices for the NE components are also listed in the Figure 14. The relationship between the angular size, flux density and spectrum of the NE component are discussed in §5.7.

## 5.2. Component Energetics

The calculation of the energetics of the NE component used the following parameters: a source distance of 2.8 kpc ( $8.6 \times 10^{16}$  km), a flux density at 1.7 GHz of 30 mJy,  $\alpha = -0.6$ , with the radio cutoff frequencies of  $10^7$  to  $10^{11}$  Hz. The volume of the component (ellipsoid of diameters  $1.5 \times 1.5 \times 0.7$  mas with the narrow dimension in the direction of the component advance) is  $6.1 \times 10^{40}$  cm<sup>3</sup>. The integrated flux density is  $6.5 \times 10^{-21}$  erg s<sup>-1</sup>cm<sup>-2</sup>, the total observed radio luminosity is  $6.1 \times 10^{30}$  erg s<sup>-1</sup>. We assume a factor of 3 to correct for the Doppler boosting of the NE component (and Doppler attenuation of 3 for the SW component) as implied by the average flux density ratio of the two component. The radio luminosity in the frame of the source is  $2.0 \times 10^{30}$  erg s<sup>-1</sup>, corresponding to a brightness temperature of about  $1 \times 10^9$  K. The total energy in relativistic particles  $E_e$ , and total energy in the magnetic field  $E_H$ , assuming the above radiating volume, are

$$E_e(\text{ergs}) = 4.0 \times 10^{37} H^{-1.5} \quad (7)$$

$$E_H(\text{ergs}) = 2.4 \times 10^{39} H^2, \quad (8)$$

where  $H$  is the magnetic field in Gauss.

The radiative lifetime of the emitting particles is about one year if magnetic field energy and kinetic energies are about equal. For example, if we assume that the protons contain 100 times the energy as the electrons, the equipartition magnetic field is about 1.0 G with a minimum total energy of  $6 \times 10^{39}$  erg in the component. If the electron energies dominate, then the minimum total energy is about  $5 \times 10^{38}$  erg and has a field strength of about 0.3 G. Such a long radiative lifetime is not possible for the NE component since it is variable on an hour time-scale and a size of  $5 \times 10^8$  km (30-min light travel time). This problem will be discussed in §5.6.

## 5.3. What is the NE component?

Emission confined to relatively discrete components, and which show relativistic motion have been observed in many Galactic X-ray binary systems (Mirabel & Rodriguez 1999). Three explanations are generally given for the energetics of these components: (1) Ejected clouds, where the components are clouds of radiating particles, expelled from the binary in a preferred direction,

but containing their own energy source; (2) Interaction within beams; where the energy flow within twin-beams is collimated by an accretion disk of the massive object and interacts with embedded matter or entrained material to produce radiating electrons; (3) a working surface where the energy flow in the efficient twin-beams is relatively invisible until the flow impinges on external material and forms a bright, small region of highly relativistic particles. The beam also penetrates through the external medium at relativistic velocities. We suggest that the moving components on opposite sides of Sco X-1 are regions of intense radio emission, generally denoted as *lobes*, formed from the interaction of a twin-beam with the ambient medium in a confined region called a *working surface*.

There are two properties of the components in Sco X-1 that that are best explained by this lobe model. First, the rapid variability and lack of systematic decay of these components implies that the radiating electrons have a lifetime of less than one hour and are constantly resupplied with energy. In fact, the NE component variability is similar to that of the core. In contrast, the emission from the relativistic moving components associated with the other well-studied Galactic-jet radio sources are not as variable and tend to decrease fairly uniformly as they move away from the radio core (Fender et al. 1999; Hjellming & Rupen 1995). Secondly, the observations of Sco X-1 suggest that only one pair of components (NE and SW) occur at any given time (see Figure 11 for a possible exception). The core does show activity and extended emission towards the northeast direction, but more than one compact component is not observed on either side of the core. For the other Galactic-jet sources, several components are usually visible on one side of the core and they are often associated with X-ray and radio flaring events in the core region.

However, the later stages of the lobe evolution in Sco X-1 did show a more complicated structure. For example, the radio emission from Sco X-1 on MJD 50872 and MJD 51054 had an extended NE component containing several bright regions. On MJD 50872 this extended NE component is clearly associated with the moving compact component observed on the previous day and consists of an

extended lobe towards the core with a few small brighter regions. Perhaps this extended emission is back flow from the lobe region seen in many extragalactic objects (Black et al. 1992).

#### 5.4. The Advance Velocity of the Lobe

The speed of advance for three different lobe-pairs were measured over the range  $0.32 < \beta < 0.57$ . The NE lobe on MJD 51340 moved at  $0.32c$  just before evaporating. The lobe on MJD 50871 moved at  $0.43c$ . The lobe on MJD 51341-2 moved initially at  $0.57c$ , but abruptly decreased to  $0.46c$  just after a lobe flare. The advance speed during each epoch was remarkably constant over periods of many hours, up to one day.

A prediction of the advance speed of the lobe requires a detailed model of the interaction of the beam with the ambient medium, A more general approach (Blandford & Königl 1979) has derived the velocity of the advance of a lobe under the assumption that the relativistic shock produces an ultra-relativistic equation of state on *both* sides of the shock. This region is generally called the *working surface* and this region produces a radio hot-spot which may be a small, but intense, part of the lobe. If  $p_1$  and  $p_2$  are the pressures and  $v_1$  and  $v_2$  are the velocities in the unshocked (beam) and shocked (working-surface) regions, then

$$\frac{v_1}{c} = \sqrt{\frac{p_1 + 3p_2}{3(3p_1 + p_2)}} \quad \frac{v_2}{c} = \sqrt{\frac{3p_1 + p_2}{3(p_1 + 3p_2)}}. \quad (9)$$

When the beam pressure is much greater than the shock pressure, the advance speed is  $0.33c$ . For more dominant shock pressure, the advance speed eventually reaches  $c$ . This model gives results which are consistent with the range of observed speeds using reasonable pressure ratios across the hot-spot. However, the small variation of the observed speed with time is still puzzling.

#### 5.5. Lobe Emission Geometry

The ultra-relativistic fluid produced at the working surface fills the larger volume of the radiating lobe. Figure 15 shows a schematic of the general appearance of the lobe based on some very simple assumptions. There are two velocities associated with the lobe: the average bulk motion velocity of  $\approx 0.45c$ , and a diffusion velocity of  $0.57c$  associated with this relativistic gas. We assume

further that the radiative lifetime of the emitting particles is about 30-minutes as required by the variability time-scale. The ‘wagon-wheel’ diameter (in the frame of the lobe) is then  $6.2 \times 10^8$  km in diameter, and the thickness is the distance traveled by the lobe in 30 minutes,  $2.4 \times 10^8$  km. The lobe, however, viewed at an angle of  $44^\circ$  to the line of sight, would make the component appear somewhat more circular than the above model.

A deeper analysis of the physical processes in the lobes requires detailed hydrodynamic jet modeling and the radiative transfer of the electrons. The modeling of (Mioduszewski et al. 1997), for example, shows striking similarities between the structure of Sco X-1 with some of their simulated models at a viewing angle of  $45^\circ$  to the line of sight (see their Figures 1d, 5c, 16a). The predicted peak brightness ratio between receding and advancing lobes is  $R=0.05$ . However, this model assumes an isotropic magnetic field distribution. In any case, there seems to be a small family of models whose parameters can be chosen to match the morphology as well as the physical properties and characteristics of the lobes.

#### 5.6. Lobe Emission Lifetime

The lifetime of the radiating plasma in the lobe cannot be much longer than 30 minutes, the variability time-scale. The two most likely sources of energy depletion are from synchrotron losses or from adiabatic expansion of the plasma. First, if equipartition holds between the magnetic energy and particle energies as discussed in §5.2, then the time scale for synchrotron losses is about one year for the equipartition field strength of about 0.5 G. The radiative lifetime decreases with as  $H^{-1.5}$ ; hence a one hour decay time requires a magnetic field strength of  $H=300$  G. The derived lobe energies are then

$$E_H(\text{ergs}) = 2 \times 10^{44} \text{ for } H= 300 \text{ G} \quad (10)$$

$$E_e(\text{ergs}) = 7 \times 10^{33} \text{ for } H= 300 \text{ G}. \quad (11)$$

The magnetic energy is then a factor of  $10^8$  larger than the equipartition value, even assuming a density of protons about 100 times that of the electrons. Magnetic field amplification just in advance of the shock has been suggested (De Young 1980; Hughes & Allen 1981), although not to this extreme. With a lobe brightness temperature  $<$

$10^9\text{K}$ , the rate from inverse-Compton losses is much less than for synchrotron losses even with this large magnetic field. Such a large magnetic field requires a lobe energy density which is about  $10^5$  times larger than the minimum energy value. The outer part of the radio lobe would also have a steeper radio spectrum than near the working surface and the 1.7 GHz angular size would be larger than that at 5.0 GHz. Unfortunately, the present observations just barely resolve the lobe at 5.0 GHz and such a spectral gradient is not observable.

The radiating electrons generated within the working surface can also rapidly lose energy if they expand adiabatically to fill the lobe region. Assuming that the radio emission is optically thin (the radio spectral index  $\alpha \approx -0.6$  is consistent with this) and neglecting the motion of the lobe for the moment, the steady-state emission profile of an expanding spherical cloud which contains a steady source of accelerated electrons within a radius  $r_0$ , the working surface region, is (Ball & Vlassis 1993; Hjellming & Han 1995)

$$S(r) = S_0(r/r_0)^{4\alpha-1} \quad (12)$$

where  $S_0$  is related to the inserted energy per unit time in the working surface volume,  $r$  is the distance from the center of the working surface. For  $\alpha = -0.6$ , the intensity at  $r/r_0 = 1.22$ , is already less than half of the intensity at the working surface. Hence the adiabatically expanding electrons need not diffuse far from the working surface in order to lose most of their energy. From the measured lobe size of about 1 mas and a diffusion speed of  $0.57c$ , the electrons will lose most of their energy in about 40 minutes. The bulk motion of the lobe is somewhat less than the diffusion speed and does not substantially change the above calculation. Adiabatic expansion does not modify the spectral index of the emission across the lobe, in contrast to the spectral steepening with synchrotron ageing. In the case of pure adiabatic expansion, the working surface is an appreciable part of the observed radio lobe.

A combination of both loss mechanisms may be operating in the lobes of Sco X-1. For example, the volume close to the working surface may have a large magnetic field which completely dominates the plasma dynamics. Further away from the working surface, adiabatic expansion may be

the dominant loss mechanism. This would reduce the total energy content needed to supply the lobe emission compared with that needed if only synchrotron losses were operating.

### 5.7. Lobe Expansion

A slow expansion of the lobe angular size over an hour or two time-scale was observed several times during the observations of Sco X-1. The best example of the expansion of a lobe was on MJD 50871 after frame 3 in Figure 14. Between frames 5 and 6 the angular size increased by a linear factor of 2.2 in 50 minutes. As discussed in the above section, for pure adiabatic expansion with a uniform input energy source, the flux density in frame 6 should have decreased  $(2.2)^{4\alpha-1}$  (Hjellming & Johnston 1988) or about 4% of that in frame 5. However, the flux density at snapshot 6 was 60% of that in snapshot 5.

Without higher resolution observations of the lobe we can only speculate on this slow lobe expansion phenomenon. Since adiabatic expansion alone would produce a much more rapid decrease of flux density than that observed, we suggest that the increasing size and decreasing intensity of the lobe reflects the energy flow and size of the working surface. The somewhat decreasing spectral index could be related to the acceleration process in the working surface, or the effect of synchrotron ageing. Note that this lobe, although decreasing in flux density at the end of MJD 50871, is present on MJD 50872 as an extended lobe along the axis of the source. Hence, this lobe was reinvigorated sometime after the end of the observations on MJD 50871. Much more data are needed in order to explain the general appearance and evolution of these components.

A similar expansion and spectral steepening of a lobe occurred during the first four hours on MJD 51340. From the images in Figure 2, the component clearly expanded, the flux density decreased and the spectral index steepened to  $-1.5$  until the component fell below the detection level of the observations.

### 5.8. Energy Flow Velocity in the Beam

Paper I we showed that the the flux density variations of the radio components have good temporal correlation when assuming a model of energy

flow from the core to the lobe where: (1) a core flare is associated with an event near the binary system (2) a burst of energy associated with this event travels down the twin-beam at a velocity of  $\beta_j$ , (3) this increased energy flux intercepts the NE and SW lobes and produces a flare.

The appropriate time delays between the NE and SW lobes with respect to the observer/core reference frame can be determined using the known lobe velocity  $\beta$  and orientation  $\theta$  to the line of sight. This model predicts the delay of the lobe flares  $\tau_{NE}$  and  $\tau_{SW}$ , with respect to the driving core flare as viewed by the observer, to be:

$$\tau_{NE} = (t_1 - t_0)\beta \frac{(1 - \beta_j \cos\theta)}{(\beta_j - \beta)}, \quad (13)$$

$$\tau_{SW} = (t_1 - t_0)\beta \frac{(1 + \beta_j \cos\theta)}{(\beta_j - \beta)}. \quad (14)$$

Here  $t_0$  is the time of ejection of the lobes from the core, and  $t_1$  is the time of a core flare. With this model, the NE lobe should flare at time  $t_1 + \tau_{NE}$  and the SW lobe at time  $t_1 + \tau_{SW}$  later than the core, as viewed by the observer. The term  $(t_1 - t_0)\beta$  is the true distance of the lobes from the core at time  $t_1$ .

Figure 16a shows the observed flux density versus time for the three components. Figure 16b shows the flux density correlations after correcting for the model delay, assuming  $\beta_j = 1$ . Figure 16c shows the same data assuming  $\beta_j = 0.90$  and the correlations between the core with the NE and SW lobe flux density flares are significantly worse. Additional discussions of the correlations and its relationship to various properties of Sco X-1 were presented in Paper I.

A lower limit to the flow speed in the beam, as indicated by the difference in correlation between Figures 16b and 16c, can be determined more quantitatively. It seems unlikely that the apparent correlations in Figure 16b are pure chance. There are three pairs of flares (C3-L3, C4-L4, C3-S3) which are clearly correlated; all are associated with a significantly different delay, using a model with only one free parameter, derived solely from the positional information of the components. The correlation of the flares for  $\beta_j = 1.0$  is clearly better than that for  $\beta_j = 0.9$  (and by symmetry for  $\beta_j = 1.1$ ), but how much better?

An estimate of the uncertainty can be obtained

by determining the speed necessary to align each of the three flare correlations (C3-N3), (C4-N4) and (C3-S3). These results yield the three independent estimates of  $\beta_j$  of  $1.10 \pm 0.10$ ,  $1.00 \pm 0.04$ , and  $1.02 \pm 0.04$  respectively, which gives a weighted average  $\beta_j = 1.02 \pm 0.04$ . Changing the space velocity of the lobes within the estimated uncertainty affects  $\beta_j$  only at the few percent level. The relatively large beam speed of  $1.10c$  associated with flare (C3-N3) may be caused by an additional delay in the flare of the core. We have suggested that the core may be at the base of the jet, at a distance of one or two mas from the binary. This would cause a delay in the core flare reaching the observer by  $\approx 0.1$  hours, compared the event in the binary system.

Thus, we derive a lower limit of  $\beta_j > 0.95$  based on the above analysis. Although the analysis indicates that this limit is significant at the two-sigma level, the model may be too simplistic. We believe that the limit has a confidence level of 70% (one-sigma).

## 5.9. Flux Density Variations and Doppler-Boosting

Based on the space motion of the lobes, we calculate that Doppler boosting will produce a flux density ratio of the SW lobe to the NE lobe of  $R=0.17$  assuming a uniformly filled lobe with an isotropic magnetic field. The observed flux density ratio is difficult to determine because of the variability of the lobes and the time delay in their reference frames. However, an estimate can be obtained by two methods. First, Figure 13 shows the distribution of the flux densities of the NE and SW components over all of the observations. At 5.0 GHz the highest flux densities observed for the NE component are about 18 mJy. For the SW component, the largest flux densities are 4.5 mJy at 1.7 GHz, which corresponds to about 2.2 mJy at 5.0 GHz assuming  $\alpha = -0.6$ . This ratio is  $R=0.12$ . A discussion of the core and its relationship to the x-ray and optical emission is given elsewhere (Geldzahler et al. 2002). Second, another estimate of the Doppler-boosting can be made from the flare peak #3 for the NE lobe and the SW lobe, shown in Figure 16. The increased flux densities at 5 GHz in the flare, compared with the baseline derived from a few hours before and after the flare, are: Core flare = 3.5 mJy, NE lobe

= 17.0 mJy, and SW lobe = 1.0 mJy. The ratio between the SW and NE lobe flare height is  $R=0.06$ . This ratio assumes that the energy flow in the twin-beams are the same. Finally, hydrodynamic modeling of a source with similar properties as Sco X-1 (Mioduszewski et al. 1997) gives suggests a ratio of  $R=0.07$  for the peaks of the simulated lobes—which is resolution dependent. All of these estimates are lower than the  $R=0.17$  expected purely from the space motion; however, any complexity in the emission properties of the lobes (eg. internal structure, non-isotropic magnetic field) tends to decrease this expected ratio (Cawthorne 1991)

### 5.10. Comparison with other Galactic-Jet Sources

Why does Sco X-1 show a lobe phenomenon when the observations of other well studied Galactic-jet sources generally show multiple components? The general consensus from the other well-studied Galactic-jet objects like GRS1915+105 (Dhawan et al. 2000, Fender et al. 1999), GRSJ1655 (Tingay et al. 1995; Hjellming & Rupen 1995), CygX-3 (Geldzahler et al. 1984; Marti et al. 1992. Schalinski et al. 1993; Mioduszewski et al. 2001), SS433 (Margon 1984; Spencer 1984), and Cir X-1 (Fender et al. 1998), is the radiating material is probably associated with discrete clouds or shocks being energized within a collimated flow of energy. Most of these objects are transient X-ray sources, preferentially observed just during or after a strong flare. These flares may be associated with the ejection of a large amount of material that is entrained in a collimated flow of energy, producing strong radio emission. However, there are several periods when the core of Sco X-1 showed changing radio emission usually within 5 mas towards the northeast. Two of these events are associated with the emergence of the new NE component on MJD 51341.0 (Figure 2) and MJD 50682.0 (Figure 11), and have already been discussed. After the core flare at MJD 51341.95 (Figure 2), extended emission to the NE persisted for about four hours. A compact NE component more than 15 mas from the core was also present. Figure 14 shows that the core on MJD 50871 was also slightly extended by about 3 mas toward the north-east direction. The extended emission near the core may be associated with material in the

beam flow.

The degenerate object associated with Sco X-1 is probably a neutron star, although the improved orbital parameters, based on the orientation of the source discussed in §4.2, do not confidently constrain the degenerate star mass to less than about  $2 M_{\odot}$ . For most other Galactic-jet sources, the degenerate star is probably too massive to be a neutron star. Sco X-1 is also a persistent X-ray source, unlike many of the other well-studied Galactic transient X-ray sources. The relationship between the X-ray properties with the nature of the degenerate star and with the properties of the radio emission is still unknown.

Finally, the major difference between Sco X-1 and the other sources may be the viewing angle of the source as seen by the observer. The simulated images (Mioduszewski et al. 1997), which showed a radio structure surprisingly similar to that seen in Sco X-1, take on the appearance of the other Galactic-jet sources when the viewing angle is decreased. At small viewing angles, the shocked material moving near  $c$  are greatly Doppler boosted and dominate over the emission from the more slowly-moving lobes. Thus, like the extra-galactic sources, the radio appearance of Galactic-jet sources may also be a strong function of viewing angle.

### 6. Comparison with Extragalactic Sources

One of the major reasons for studying Galactic-jet sources is to understand better the jet phenomenon in extragalactic radio sources. The appropriate scaling laws come from considerations of the accretion disks and infalling mass (Begelman et al. 1984). The radio emission is a second order product of the accretion process, but should also follow the scaling. The luminosity ratio of Sco X-1 to Cygnus A, for example, is  $10^{-7}$ . The mass ratio of the neutron star in Sco X-1 and the massive object in Cygnus A is  $10^{-9}$ . We will adopt as a typical scaling parameter  $x$ , from a radio galaxy to Sco X-1  $x \approx 10^{-8}$ . The luminosity, the time scale and the size will scale as  $x$ , the density as  $x^{-1}$ , the magnetic field as  $x^{-0.5}$ , and velocity and temperature are invariant to first order. The following are some examples of simple scaling of the properties of Sco X-1's radio lobes to those in extragalactic radio sources.



Two of the best studied extragalactic radio sources with strong lobes are Cygnus A (Carilli et al. 1991) and Pictor A (Perley et al. 1997). Comparisons of these and other sources with Sco X-1 indicates:

- **Lobe Variability.** The lobes in Sco X-1 vary on an hour time scale. This scales to  $1 \times 10^4$  yr for radio galaxies. Variability in extragalactic lobes have not yet been observed over about a 30-year span.
- **Lobe Lifetime.** The lifetime for a pair of lobes in Sco X-1 is about one day. This scales to  $5 \times 10^5$  yr for a typical extragalactic source, and is about the estimated age of the Cygnus A hot spots, based on the curvature of their radio spectrum (Carilli et al. 1991; Cox et al. 1991).
- **Lobe Regeneration.** In Sco X-1 there appears to be replenishment of the radio lobes. That is, after a pair of lobes fades away, another pair emerges from the core, probably in less than one day. The one well-documented disappearance of the lobes (MJD 51840) occurs after an X-ray flare and the emergence of an optically-thick core component. The suggestion that the the beam flow has been disrupted and later reforms is discussed elsewhere (Geldzahler et al. 2002). Although a short lifetime of  $10^5$  yr for hot-spots in radio galaxies has been suggested from lobe modeling (Cox et al. 1991) and observations of radio galaxy lobes (Black et al. 1992), new hot-spots are believed to appear in the established radio-lobe region rather than being reformed near the core. Hence, unlike Sco X-1, the beam flow in extragalactic sources may not be completely disrupted.
- **Lobe Size.** The linear size of the lobe in Sco X-1 of  $2 \times 10^8$  km scales to 500 pc for radio galaxies, similar to that observed in radio galaxies (Black et al. 1992). The western lobe in Pictor A (Perley et al. 1997) is well-resolved and is somewhat more elongated perpendicular to the presumed input energy flow, as found for Sco X-1.
- **Lobe Distance from Core.** The lobe separation of Sco X-1 is about 40 mas or

$1.6 \times 10^{10}$  km. This scales to a linear size of  $1.6 \times 10^{18}$  km or 50 kpc for the typical size of a radio galaxy.

- **Spectral Index.** The spectral indices associated with the lobes of Sco X-1 are similar to those seen in extragalactic sources, where the most confined lobes have  $\alpha \approx -0.5$  and the less confined have steeper spectral index.
- **Opening angle.** The ratio of the lobe size to the distance from the core is probably related to the angle opening in the beam. For Sco X-1 this angle is typically about  $1^\circ$ . A similar ratio is observed for extragalactic double sources that have prominent hot-spots in their radio lobes.
- **Magnetic Field Strength.** The equipartition magnetic field in Sco X-1 was  $\sim 1$  G. If adiabatic expansion of the plasma in the lobes is not occurring, the field needed to decrease the electron emitting lifetimes from synchrotron losses to one hour was  $\sim 300$  G. These two magnetic fields strengths scale to  $1 \times 10^{-4}$  G (which is similar to the equipartition field in Cygnus A) and  $3 \times 10^{-2}$  G respectively. The configuration of the magnetic field in the lobes of Pictor A appears to be circumferential (Perley et al. 1997). The degree of polarization in Pictor A is also high, indicating an ordered field. No lobe polarization information is available for Sco X-1. However, if the lobes are dynamically controlled by a large magnetic field, a radial magnetic field would be more likely with Sco X-1.

A major difference between the radio lobes of Sco X-1 and those associated with radio galaxies is the apparent simplicity of the Sco X-1 lobes, usually consisting of two hot-spots and no extended emission. In contrast, radio galaxies often show an extended lobe, with a cocoon of emission, and a hot-spot. Emission from the beam between the core and the lobe is also observed in some cases. Often a secondary hot-spot is observed in a radio lobe, not far from the more compact one. These secondary hot-spots are thought to be caused by either the splatter of material from the primary hot-spot, or the remnants of older hot-spots which are still radiating (Cox et al. 1991).

The difference in appearance between Sco X-1 and a typical radio galaxy is *not* the result of the high dynamic range images available for many extragalactic sources. Even at the modest dynamic range of the Sco X-1 images (peak flux density to rms noise level of about 50) nearly all double radio sources have more complicated lobes than that observed in Sco X-1. Perhaps the suggested strong magnetic field in Sco X-1 confines the relativistic fluid to a small region. In contrast, on MJD 50872 and MJD 51054 the NE lobe of Sco X-1 resembled the morphology of that in FR II-type radio galaxies. The lobe was extended along the source axis and the hot-spot was not dominant. For the MJD 50872 observations, we know that the lobe was formed more than 1.5 days earlier, suggesting that the confinement of relativistic particles within a small region is less likely as Sco X-1 evolves.

Explanations for the differences seen between the radio lobes in Sco X-1 and those of extragalactic sources require a better understanding of the formation of the working-surface and the relativistic particles and fields and their transport into the hot-spot. One significant difference between Sco X-1 and radio galaxies may be the advance speed of the hot-spot. For Sco X-1, the advance velocity is  $0.5c$ . It is believed that the advance velocity in radio galaxies is only mildly relativistic  $\approx 0.1c$ . Another difference may be that the lobes in extragalactic sources are probably confined by ram pressure. In Sco X-1, the lobes may be confined by a strong magnetic field, or, not confined at all with adiabatic expansion occurring outside of the working surface region.

## 7. Conclusion

These extensive VLBI observations of Sco X-1 are among the most detailed for a Galactic-jet radio source. The high-resolution images over the four-year study show relativistic motion and variability of all components and a recurrent phenomenon of lobe production. The resolution and sensitivity are sufficient to determine accurate parameters of the discrete components as a function of time. Since we have observed Sco X-1 without regard to its X-ray and radio flux density, we may be sampling the more stationary properties of a Galactic-jet source rather than those associ-

ated with the evolution during the more explosive periods.

The relatively non-speculative conclusions from these observations are the following.

- Sco X-1 is composed of three components: a radio core near the compact component, a NE component which moves away from the core, and a weaker SW component which is detected about half of the time.
- Occasionally weak extended emission emanates from the core in the north-eastern direction, but generally only a NE and SW component are detected.
- All components are variable on time scales of about one hour. The rapid increase and somewhat less rapid decrease in the flux density for all of the components has a characteristic time scale of about three hours. This time-scale of the radio variations in Sco X-1 has already been noted (Hjellming et al. 1990; Bradshaw et al. 1997).
- A pair of moving components persists up to about two days. Recurrent generation of pairs occurs often enough that a naked core component is not commonly observed.
- The comparison of the radio properties between the NE and SW components strongly suggest that they are intrinsically similar, but differ from the effects of relativistic aberration and Doppler beaming.
- The average speed of the NE and SW components is  $0.45c \pm 0.03c$ , radially away from the core at an angle  $44^\circ \pm 7^\circ$  to the line of sight.
- The component speeds remain unchanged for many hours although the speeds for different pairs of components at different times range between  $0.31c$  and  $0.57c$ .
- The components of Sco X-1 lie on a axis which has not varied by more than about  $4^\circ$  over five years. A variation of axis direction of  $\approx 3^\circ$ , with a period of a few days, may be present.

- The minimum angular size of the NE (and presumably the SW) component is  $1.5 \times 0.7$  mas ( $6 \times 310^{13}$  cm) with an orientation *perpendicular* to the motion of the lobe. This corresponds to a volume of  $6.1 \times 10^{40}$  cm<sup>3</sup>. The equipartition magnetic field is between 0.3 to 1.0 G depending on the ratio of electrons to protons.
- The lobes of Sco X-1 are dominated by a compact hot-spot. The lobes of most extragalactic sources often contain one or more hot-spots and much more extended structure.

More speculative conclusions are:

- The NE and SW components are lobes generated from a working surface where the energy flow within a twin-beam from the binary impinges on the ISM. This conclusion is based on the variability of the components, the lack of a systematic decrease in the lobe flux density with time, and the simplicity of the components.
- If the above suggestion is correct then the temporal correlation of the core flare times with those of the NE lobe and SW lobe suggest a beam velocity  $> 0.95c$ .
- In Sco X-1 the lobe emission dominates. In most other Galactic-jet sources, emission from material or shocks within the jets dominate. This may be an intrinsic difference between the sources, perhaps related to either the nature of the degenerate star or the persistence of the X-ray emission. Alternatively, the difference may be associated with the angle between the observer and the direction of source motion.
- The variability of the lobes and their linear size suggest a radiative lifetime of less than one hour. For synchrotron losses in the emitting plasma, a magnetic field of  $\sim 300$  G is needed, which implies a lobe dominated by magnetic energy. Alternatively, an adiabatic expansion of the ultra-relativistic plasma, after generation at the working surface, is also consistent with the lobe emission characteristics.

- The simple pressure balance in the ultra-relativistic plasma on both sides of the shock at the working surface predicts an advance speed of the lobe in the range of that observed. The relatively constant speed of the lobes over many hours is surprising and no explanations are offered.
- The lobe looks like a wagon wheel. The working surface is at the hub and the electrons diffuse with  $0.57c$  away from the working-surface shock. The advance of the lobe over the lifetime of the radiating electrons (30 minutes) also contributes to its size in the direction of motion.
- The slow expansion of the lobes, with a decrease in flux density and steepening spectrum, may be associated with a decreasing beam flow and enlarging of the working surface, as well as from adiabatic expansion of material in the lobes.
- The ‘scaling’ of the Sco X-1 phenomena to that of radio galaxies suggests that hot-spot variability and life-times may be only  $10^5$  yr in radio galaxy lobes.

These observations show that VLBI resolutions are sufficient to determine the internal properties of Galactic-jet radio sources. The time scales of the evolution vary from less than one hour to a few days or months in some cases. Hence, detailed, long-term, multi-frequency and reasonably continuous observations are required to follow and understand the emission properties of the sources. Because of the possible dominant effect of the magnetic field, linear polarization imaging would be very useful.

The National Radio Astronomy Observatory is a facility of the National Science Foundation, operated under cooperative agreement by Associated Universities, Inc. We thank the European VLBI Network (EVN) and the Asia-Pacific Telescope (APT) for their support and observation time. The data were correlated with the VLBA correlator in Socorro and the Penticton Correlator that is supported by the Canadian Space Agency. It is a pleasure to thank Dr. Jean Swank for granting us RXTE time, to Dr. Tasso Tzioumis for help with

the APT scheduling, and to Dr. Sean Dougherty for processing the APT data. We thank Dr. Michael McCollough and Dr. Vivek Dhawan for comments on the draft.

## REFERENCES

- Ables, J. G. 1969, *Proc ASA*, 1, 273
- Ball, L. & Vlassis, M., 1993, *Proc ASA*, 10, 4
- Bandyopadhyay, R. M., Shahbaz, T., Charles, P. A. & Naylor, T. 1999, *MNRAS*, 306, 417
- Begelman, M. C., Blandford, R. D. & Rees, M. J. 1984, *Rev. Mod. Phys.*, 56, 255
- Black, A. R. S., Baum, S. A., Leahy, J. P., Perley, R. A., Riley, J. M., & Scheuer, P. A. G. 1990, *MNRAS*, 256, 186
- Blandford, R. D. & Königl, A. 1979, *ApJ*, 232, 34
- Blandford, R. D. , McKee, C. F. & Rees, M. J. 1977, *Nature*, 267, 211
- Blandford, R. D. & Rees, M. J. 1974, *MNRAS*, 169, 395
- Bradshaw, C. F., Geldzahler, B. J. & Fomalont, E. B. 1997, *ApJ*, 481, 489
- Bradshaw, C. F., Fomalont, E. B. & Geldzahler, B. J. 1999, *ApJ*, 512, L121
- Bradshaw, C. J., Geldzahler, B. J., & Fomalont, E. B., 2002, in preparation.
- Carilli, C. L., Perley, R. A., Dreher, J. W. & Leahy, J. P. 1991, *ApJ*, 383, 554
- Cawthorne, T. V. 1991, in *Beams and Jets in Astrophysics*, ed. P. A. Hughes (Cambridge: Cambridge Univ. Press), 187
- Cox, C. I., Gull, S. .F. & Scheuer, P. A. G. 1991, *MNRAS*, 252, 558
- Cowley, A. P. & Crampton, D. 1975, *ApJ*, 201, L65
- De Young, D. S., 1980. *ApJ*, 241, 81
- Dhawan, V. Mirabel, I. F. & Rodriguez. L. F. 2000, *ApJ*, in press.
- Fender R., Spencer, R., Tzioumis, T., Wu, K., van der Klis, M., van Paradijs, J. & Johnston, H. 1998, *ApJ*, 506, L121.
- Fender, R. P., Garrington, S. T., McKay, D. J., Muxlow, T. W. B., Pooley, G. G., Spencer, R. E., Stirling, A. M. & Waltman, E. B. 1999, *MNRAS*, 304, 865.
- Fomalont, E. B. & Geldzahler, B. J. 1991, *ApJ*, 383, 289.
- Fomalont, E. B., Geldzahler, B. J., & Bradshaw, C. J. 2001, *ApJletters*, in press. (Paper I)
- Geldzahler, B. J., Fomalont, E. B. & Bradshaw, C. J., 2002, in preparation.
- Geldzahler, B. J., Fomalont, E. B., Hilldrup, K. & Corey, B. E. 1981, *AJ*, 86, 1036
- Geldzahler, B. J. et al., 1983, *ApJ*, 273, L62
- Gottlieb, E. W., Wright, E. L. & Liller, W. 1975, *ApJ*, 195, L33
- Greisen, E. W., 1988, in *Acquisition, Processing and Archiving of Astronomical Images*, ed. G. Longo & G. Sedmak (Napoli: Osservatorio Astronomico di Capodimonte), 125
- Hasinger, G. & van der Klis, M. 1989, *A&A*, 225, 79
- Hjellming, R. M. & Han, X. 1995, in *X-Ray Binaries*, ed. W. G. Lewin, J. van Paradijs & E. P. van den Heuvel (Cambridge: Cambridge Univ. Press), 308
- Hjellming, R. M. & Johnston, K. J. 1988, *ApJ*, 328, 1988
- Hjellming, R. M. & Rupen, M. P., 1995, *Nature*, 375, 464
- Hjellming, R. M., Stewart, R. T., White, G. L. et al. 1990, *ApJ*, 365, 681
- Hjellming, R. M. & Wade, C. M. 1971, *ApJ*, 158, L155.
- Hughes, P. A. & Allen, A. J. 1981, *MNRAS*, 196, 339

- van der Klis, M., Swank, J. H., Zhang, W., Jahoda, K., Morgan, E. H., Lewin, W. H. G., Vaughan, B. & van Paradijs, J. 1996, *ApJ*, 469, L1
- Lamb, F. K. 1989, in Proc. 23d ESLAB Conf on X-Ray Astronomy, Vol. 1 ed. J. Hunt & B. Batrick (Paris: ESA), 215
- Lewin, W. H. G, van Paradijs, J. & van den Heuvel, E. P. J. 1995, *X-Ray Binaries: Cambridge Univ Press*, London
- Mioduszewski, A. J., Hughes, P. A. & Duncan, G. C. 1997, *ApJ*, 476, 649.
- Mioduszewski, A. J. et al. *ApJ*, in press
- Margon, B. A. 1984, *A&A Rev.*, 22, 507
- Marti, J. , Parades, J. M. & Estalella, R. 1992, *A&A*, 258, 309.
- Mirabel, I. F. & Rodriguez, L. F. 1999, *A&A Rev.*, 37, 409
- Penninx, W. 1989, in Proc. 23d ESLAB Conf on X-Ray Astronomy, Vol. 1 ed. J. Hunt & B. Batrick (Paris: ESA), 185
- Perley, R. A., Röser, H-J & Meisenheimer, K. 1997, *A&A*, 328, 12
- Schalinski, C. J., Johnston, K. J., Witzel, A. et al., 1993, *ApJ*, 447, 59.
- Shepherd, M.C. 1997, in ASP Conf. Ser. 125, *Astronomical Data Analysis Software and Systems VI*, ed. G. Hunt, & H.E. Payne (San Francisco: ASP), 77
- Spencer, R. E. 1984, *MNRAS*, 209, 869
- Tingay, S.J. et al. 1995, *Nature*, 374, 141.
- Titarchuk & Osherovich, 2000. *ApJ*, 527, L39
- Titarchuk, L. G., Bradshaw, C. F., Geldzahler, B. J. & Fomalont, E. B. 2001, in preparation.
- Vrtilek, S. D., Penninx, W., Raymond, J. C., Verbunt, F., Hertz, P., Wood, K., Lewin, W. H. G. & Mitsuda, K. 1991, *ApJ*, 376, 278
- Westphal, J. A., Sandage, A. & Kristian, J. 1968, *ApJ*, 154, 139

TABLE 1  
THE VLBI OBSERVATIONS OF SCO X-1

Date	MJD	UT range	Array	Freq (GHz)	BW (MHz)	Flux Dens. (mJy)
19-Aug-1995	49948	23.7 to 26.7	VLBA	4.98	64	0.4
16-Mar-1996	50158	10.1 to 13.0	VLBA	4.98	64	0.6
14-Sep-1996	50340	22.1 to 25.0	VLBA	4.98	64	4.5
03-Aug-1997	50663	23.9 to 29.3	VLBA	4.98	64	3.5
21-Aug-1997	50681	22.8 to 27.8	VLBA+Y1	4.98,1.67	128	15.0
27-Feb-1998	50871	10.3 to 16.0	VLBA+Y1	4.98,1.67	128	22.0
28-Feb-1998	50872	10.2 to 16.0	VLBA+Y1	4.98,1.67	128	5.0
29-Aug-1998	51054	23.8 to 27.0	VLBA+Y1	4.98,1.67	128	9.0
11-Jun-1999	51340	02.2 to 10.2	VLBA+Y27	4.98,1.67	128	20.0
11-Jun-1999	51340	10.2 to 18.2	APT <sup>1</sup>	4.98	64	8.0
11-Jun-1999	51340	18.2 to 26.2	EVN+ <sup>2</sup>	4.98	128	18.0
12-Jun-1999	51341	02.2 to 10.2	VLBA+Y27	4.98,1.67	128	14.0
12-Jun-1999	51341	10.2 to 18.2	APT <sup>1</sup>	4.98	64	12.0
12-Jun-1999	51341	18.2 to 26.2	EVN+ <sup>2</sup>	4.98	128	14.0
13-Jun-1999	51342	02.2 to 10.2	VLBA+Y27	4.98,1.67	128	8.0

NOTE.—

Y1 = One VLA telescope; Y27 = The entire VLA

<sup>1</sup> The APT consists of Australian Telescope Compact Array, Ceduna, Hartebeesthoek Radio Astronomical Observatory, Hobart, Kashima, Parkes, Shanghai.

<sup>2</sup> The EVN+ consists of Effelsberg, Green Bank 140', Hartebeesthoek Radio Astronomy Observatory, Jodrell Bank, Medicina, Noto, Onsala, Westerbork.

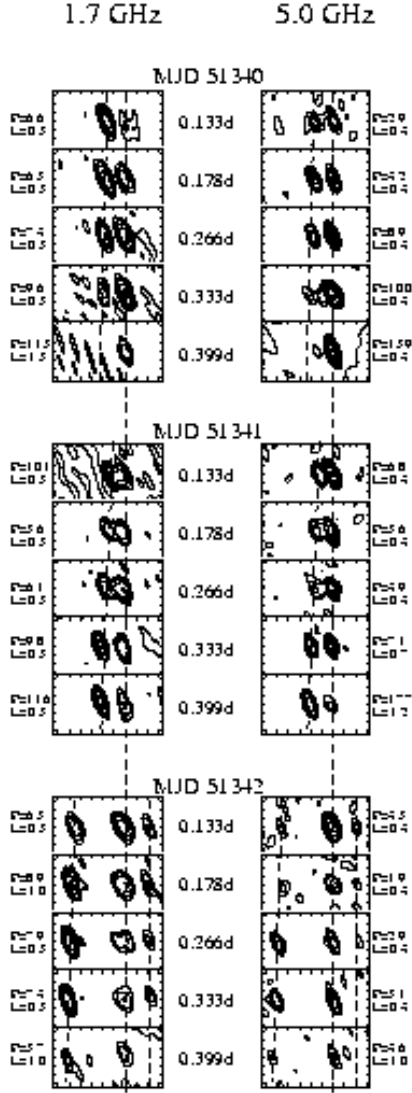


Fig. 1.— Images at 1.7 and 5.0 GHz with  $10 \times 5$  mas Resolution during 1999 June Observation. Five images, rotated  $36^\circ$  counter-clockwise in the sky, at 1.7 GHz (left) and 5.0 GHz (right), are shown for each seven-hour period on three consecutive days. The time of each snapshot is shown between the columns. An unresolved component will have a position angle of  $36^\circ$ . The minimum contour level (L) and peak flux density (P) in mJy are shown next to each plot. The contour levels are  $-1, 1, 2, 4, 8 \dots$  times the minimum level. The tick mark are separated by 10 mas on the abscissa and 5 mas on the ordinate. The scale is slightly different on the two axes. The dashed lines show the location of the core, NE and SW components.

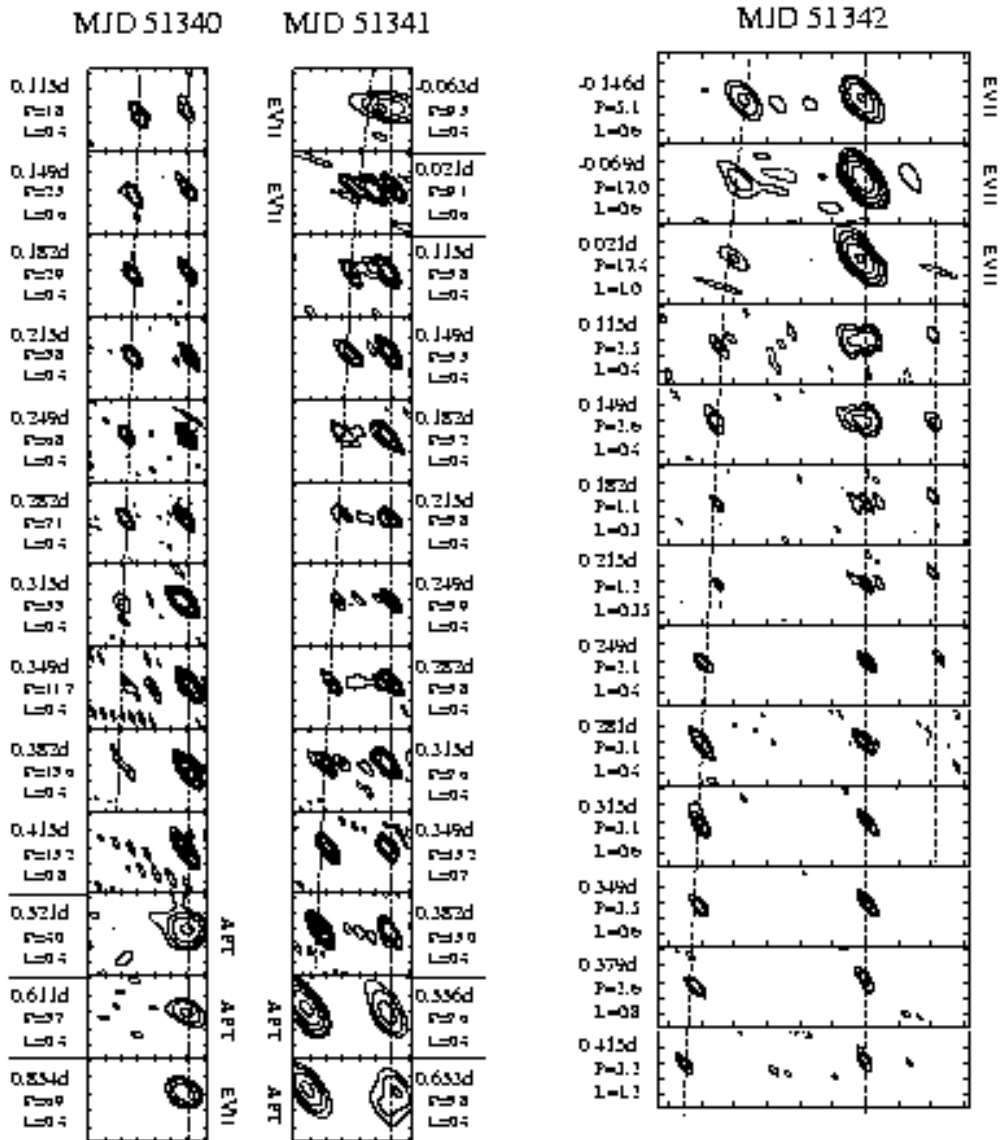


Fig. 2.— Images at 5.0 GHz with  $4 \times 2$  mas Resolution during 1999 June Observations. Thirteen images of Sco X-1, rotated  $36^\circ$  clockwise, are shown for each of the three observing days. The time of each snapshot, the peak flux density (P) in mJy and the minimum contour level (L) are given next to each plot. The contour levels are -1, 1, 2, 4, 8 ... times the minimum level. The tick marks are separated by 5 mJy, except for the abscissa on MJD 51342 where they are separated by 10 mJy. The dashed lines show the location of the core, the NE component and the SW component on MJD 51342. The images from the EVN and APT are labeled. Others come from the VLBA.



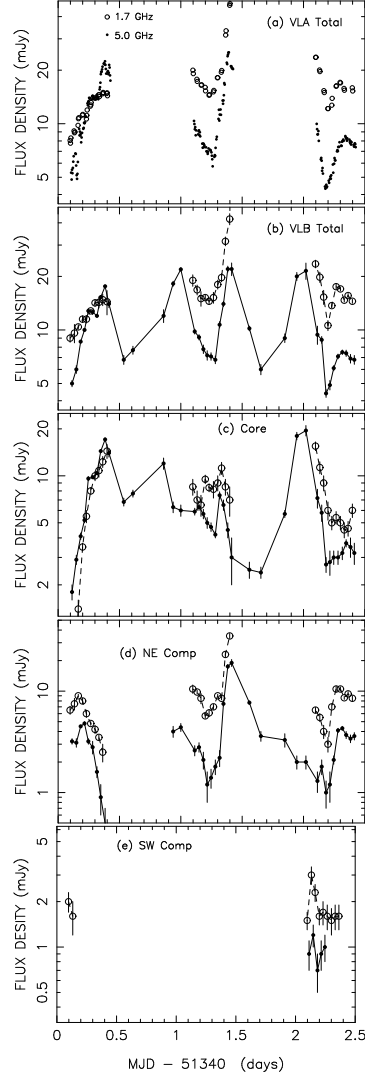


Fig. 3.— **Flux Density During 1999 June Observations.** (a) Total Flux Density from VLA, (b) Total Flux Density from VLBI, (c) Core Flux Density, (d) NE Component Flux Density, (e) SW Component Flux Density. The flux densities at 1.7 GHz are shown by the (○) points, 5.0 GHz by the (●). The flux density scale is logarithmic, hence the flux density difference between frequencies is proportional to the spectral index. The one-sigma error bars are indicated.

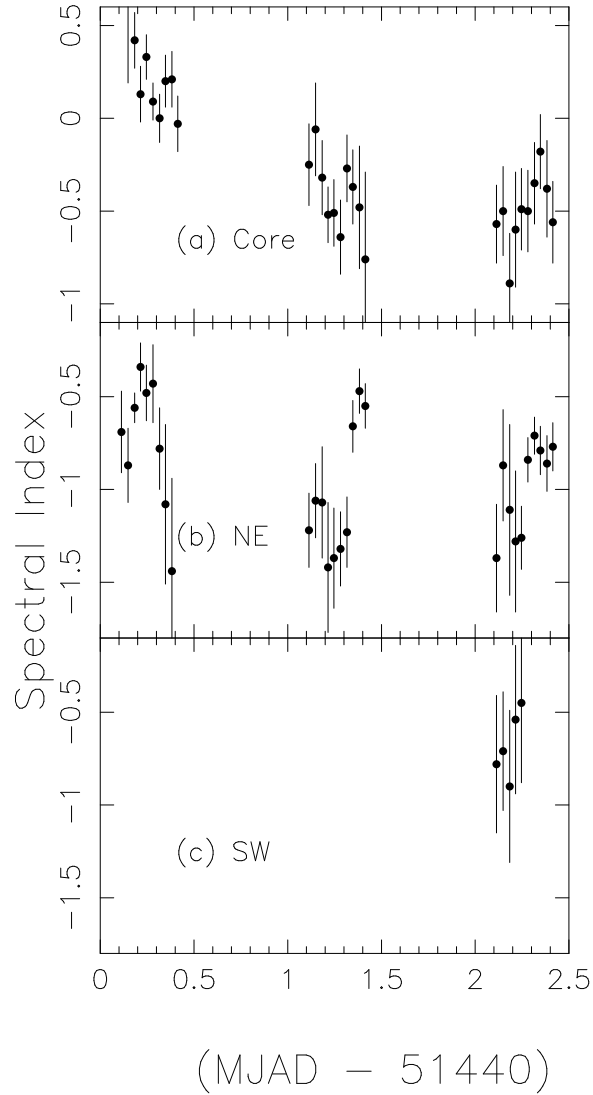


Fig. 4.— **The Spectral Index During the 1999 June Observations for the Three Main Components.** (a) Core, (b) NE Component and (c) SW component. The spectral indices are calculated only where a detection at 1.7 GHz and 5.0 GHz was made. The error bars indicate the one-sigma error.

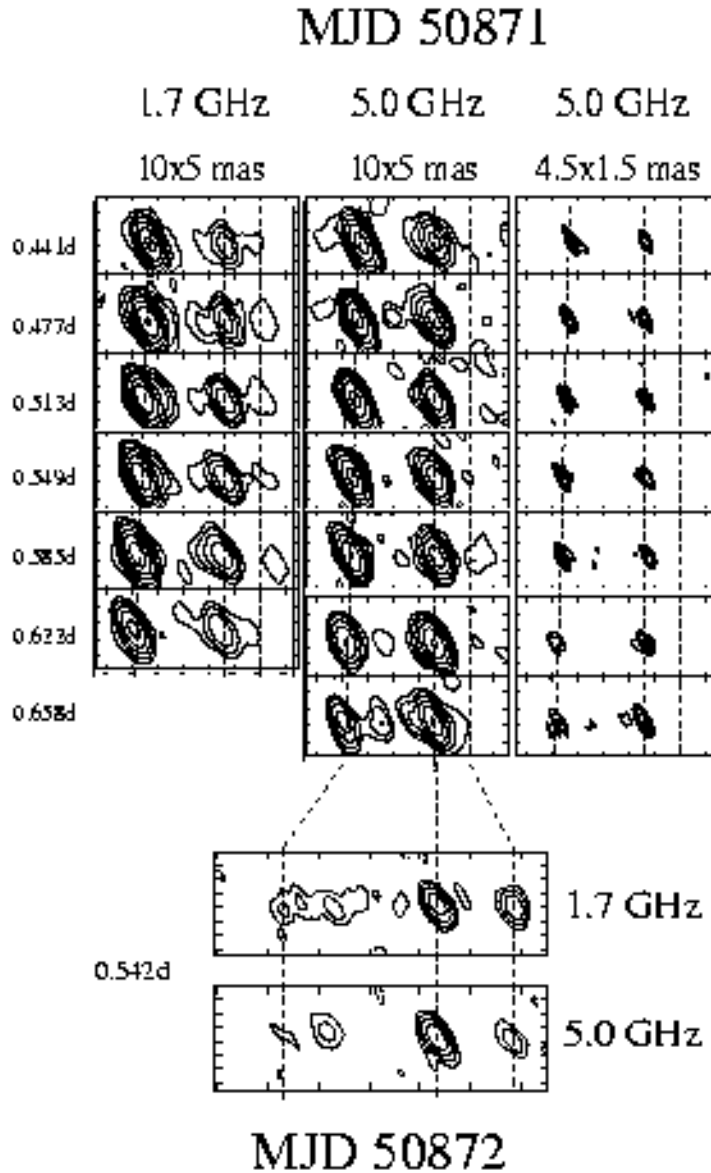


Fig. 5.— **Images During 1998 February Observations.** The upper part of the figure shows seven snapshot images on MJD 50871, rotated by  $36^\circ$  on the sky, at the frequency and resolution indicated. The minimum contour levels are 0.5, 0.4, 0.8 mJy for columns 1, 2 and 3 respectively, with contour levels at  $-1, 1, 2, 4, 8 \dots$  times the minimum level. The tick marks are separated by 10 mas on the abscissa and 5 mas on the ordinate. The lower part of the figure shows an image of Sco X-1 on the following day at 1.7 GHz and 5.0 GHz, each with a minimum contour level of 0.2 mJy. The image scale is the same as for the previous day but the tick marks on the abscissa are 20 mas.

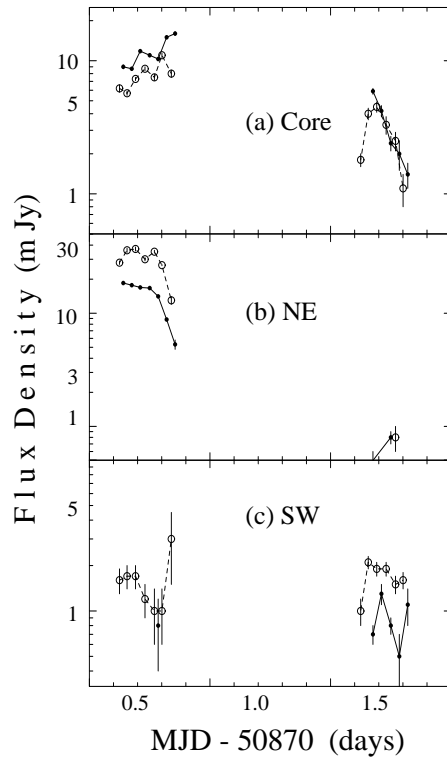


Fig. 6.— **Flux Density During 1998 February Observations for the Three Components.** (a) Core, (b) NE Component and (c) SW component. Flux densities at 1.7 GHz are shown by the (○) points, 5.0 GHz by the (●) points. The flux density scale is logarithmic and one sigma error bars are indicated. The points at each frequency are separated by 50 minutes.

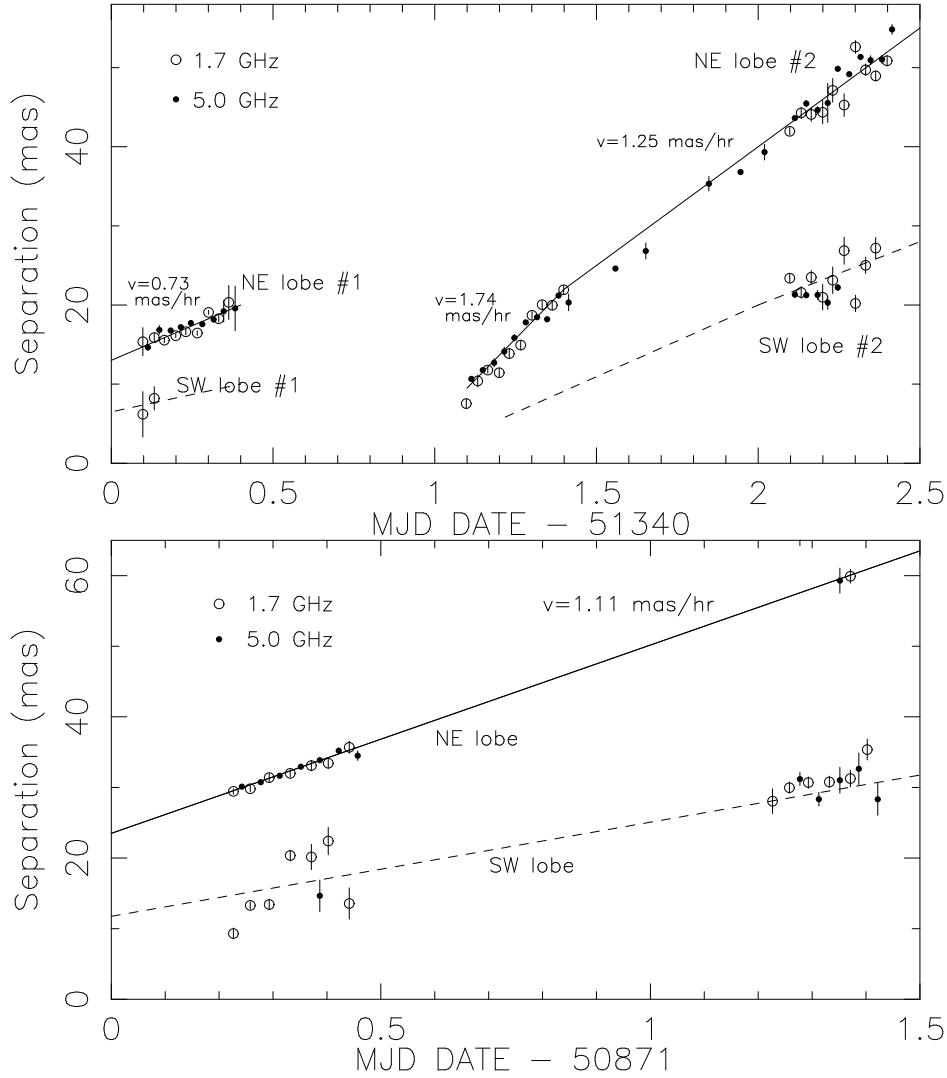


Fig. 7.— **The Velocity of the NE and SW Components.** (top) 1999 June observations and (bottom) 1998 February observation: The points show the separation of the NE and SW components from the core NE component during the observations. The best linear velocity fit for NE component #1 and component #2 in 1999 June and for the NE component in 1998 February are indicated by the solid lines. The dashed lines through the SW components are exactly 50% of that of the NE component at the same time.

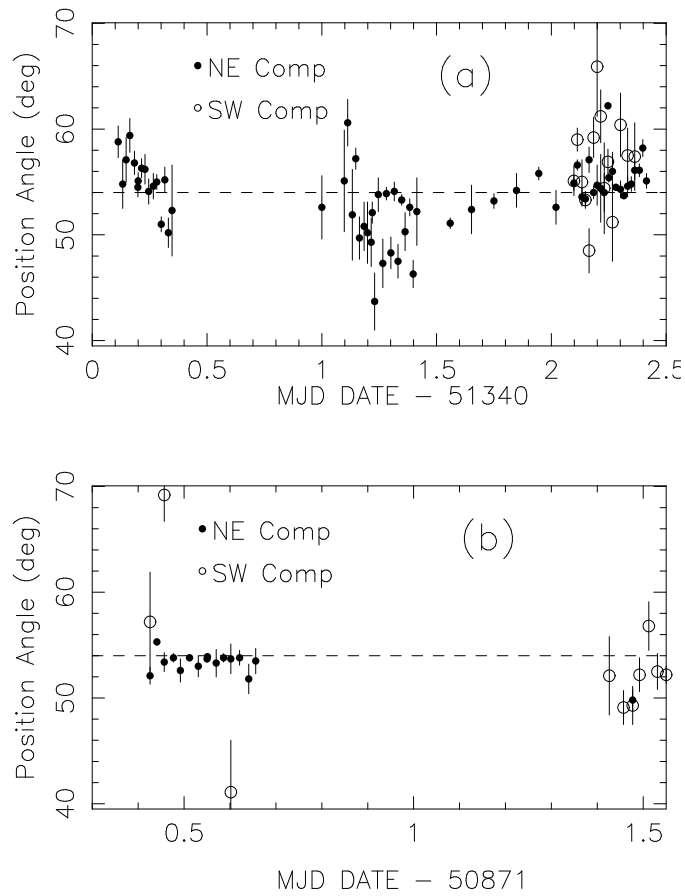


Fig. 8.— **The Position Angle of the NE and SW Components.** (a) The June 1999 observations and (b) the Feb 1998 observations. The position angle and error estimate of separation from the core for the NE components (•) and SW components (◦) are plotted separately. Position angles from both the 1.7 GHz and the 5.0 GHz observations are plotted. The dashed-line is at the weighted average position angle  $54^\circ$ .

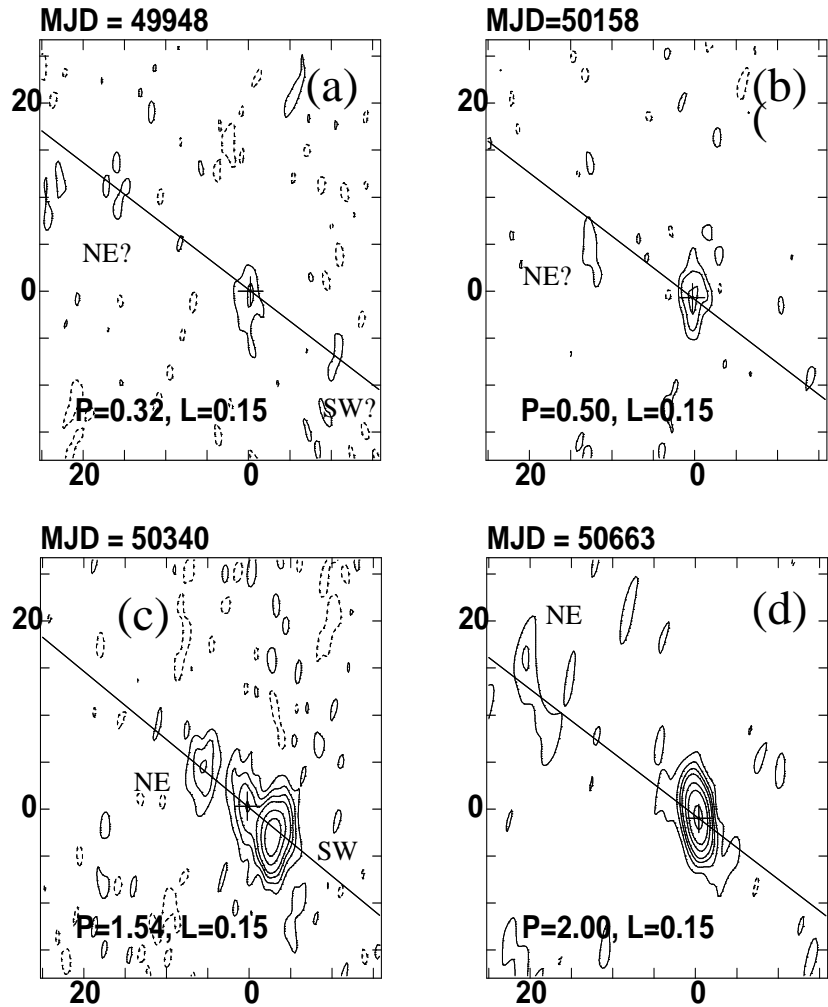


Fig. 9.— Images at 5.0 GHz for the first four observation. (a) MJD 49948, (b) MJD 50158, (c) MJD 50340 and (d) MJD 50663. The peak flux density and lowest contour level are shown in each diagram, with contour levels at -1,1,2,3,4,6,8,12 times the lowest level. The cross shows the expected location of the core position as determined from the radio parallax and proper motion analysis from all observations. The diagonal line is at position angle  $54^\circ$ . Identification of the NE and SW components (sometimes tentative) are indicated. The resolution of each image is  $6 \times 2$  mas.

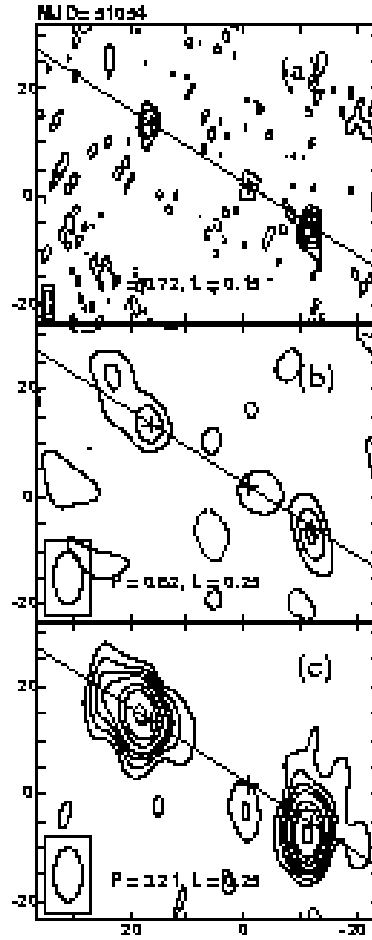


Fig. 10.— **Images on August 29, 1998.** (a)  $4.5 \times 1.5$  mas resolution image at 5.0 GHz, (b)  $10 \times 5$  mas resolution image at 5.0 GHz and (c)  $10 \times 5$  mas resolution image at 1.7 GHz. The peak flux density and lowest contour level are shown in each diagram, with each diagram indicated the resolution.



# MJD 50682

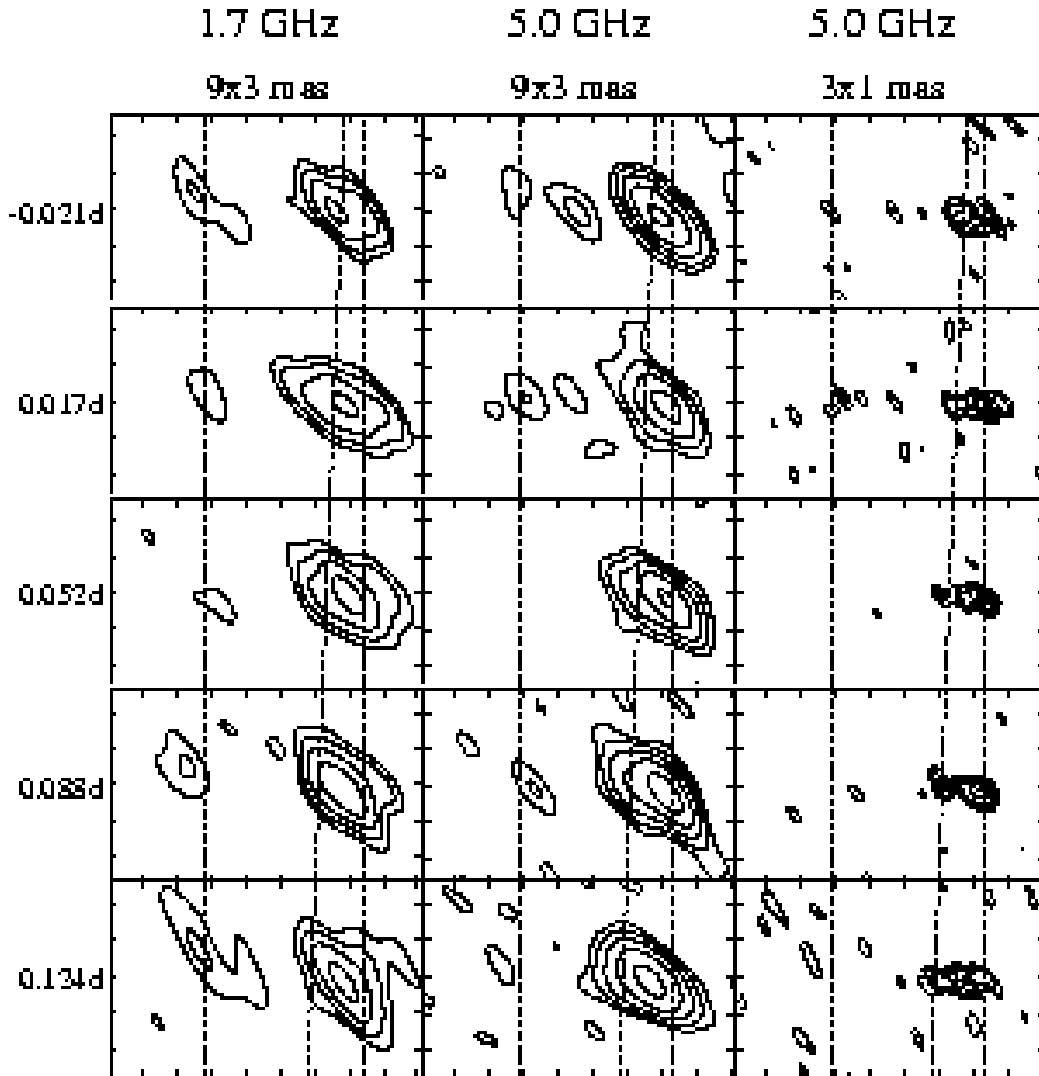


Fig. 11.— **Images on August 22, 1997.** (left)  $9 \times 3$  mas resolution images at 1.7 GHz, (middle)  $9 \times 3$  mas resolution images at 5.0 GHz and (right)  $3 \times 1$  mas resolution images at 5.0 GHz. All images have been rotated  $36^\circ$  counter-clockwise. The contour levels are  $-1, 1, 2, 4, 8 \dots$  times the minimum contour level of 0.5, 0.4, 0.7 mJy from left to right respectively. The tick mark separation is 5 mas in each coordinate. The vertical dashed line on the left of each frame is the core position. The slightly non-vertical dashed line indicated the approximate location of the NE component. The dashed line to the left in each frame is the location of a possible faint relic NE component.

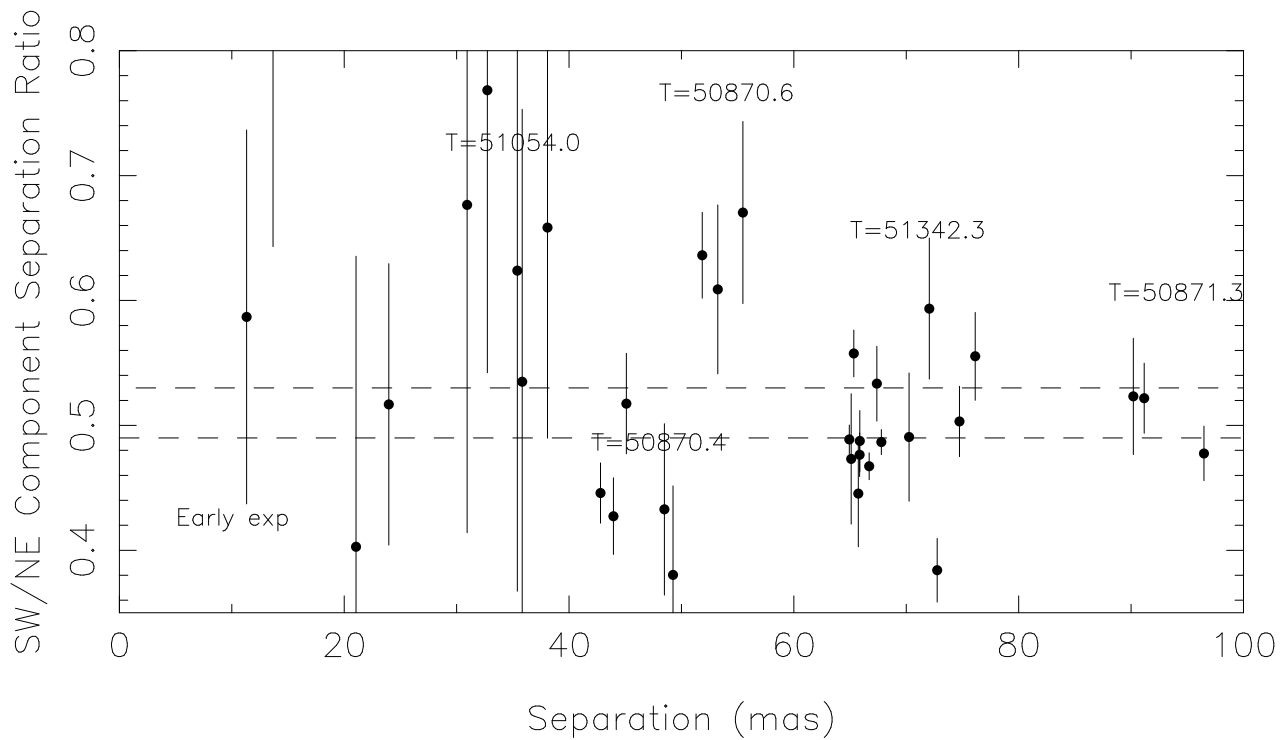


Fig. 12.— **The Distance Ratio for the SW and NE Components.** The ordinate is the ratio of the core-SW component separation divided by the core-NE component separation. The abscissa is the total separation between the NE and SW components. The observation date (MJD= $T$ ) is indicated for the clumps of points, and the error bars indicate the estimated error. The ratio  $0.51 \pm 0.02$  is indicated by the dashed-lines. This value is the mean value and error estimate, heavily weighted by the 1998 February and 1999 June Observations.

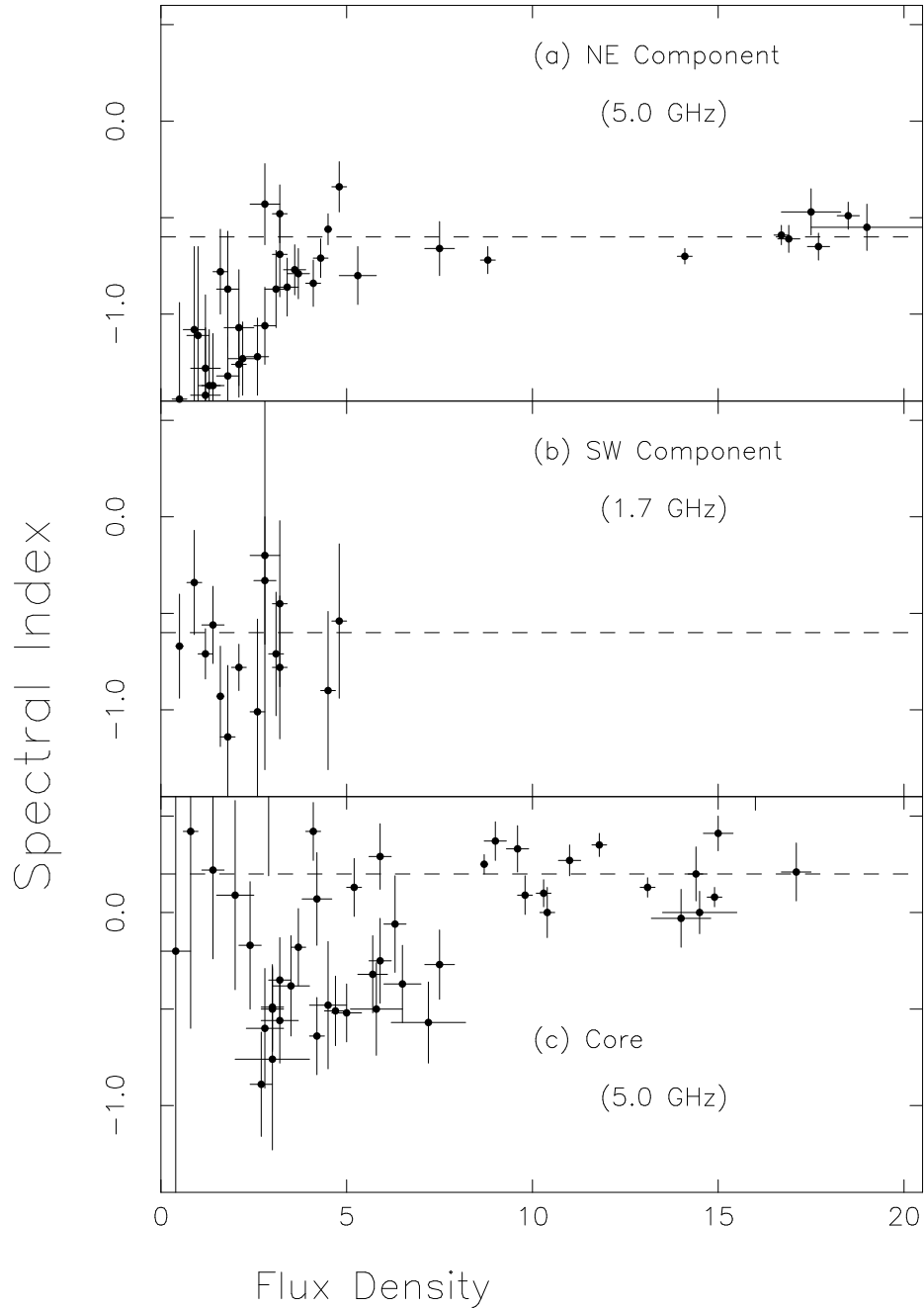


Fig. 13.— **The Spectral Index vs Flux Density for the Components.** (a) The NE component at 5.0 GHz, (b) The SW component at 1.7 GHz and (c) The Core at 5.0 GHz. The spectral index  $\alpha$  ( $S \propto \nu^\alpha$ ) is plotted versus the flux density ( $S$ ) of each component. Most of these data are from the 1999 June and 1998 February observations. The dashed line is at  $\alpha = -0.6$  for (a) and (b), and  $\alpha = +0.2$  for (c). The error bars show the estimated spectral index and flux density errors for each point. The data are shown at 1.7 GHz for the SW component since it was detected more often at this frequency.

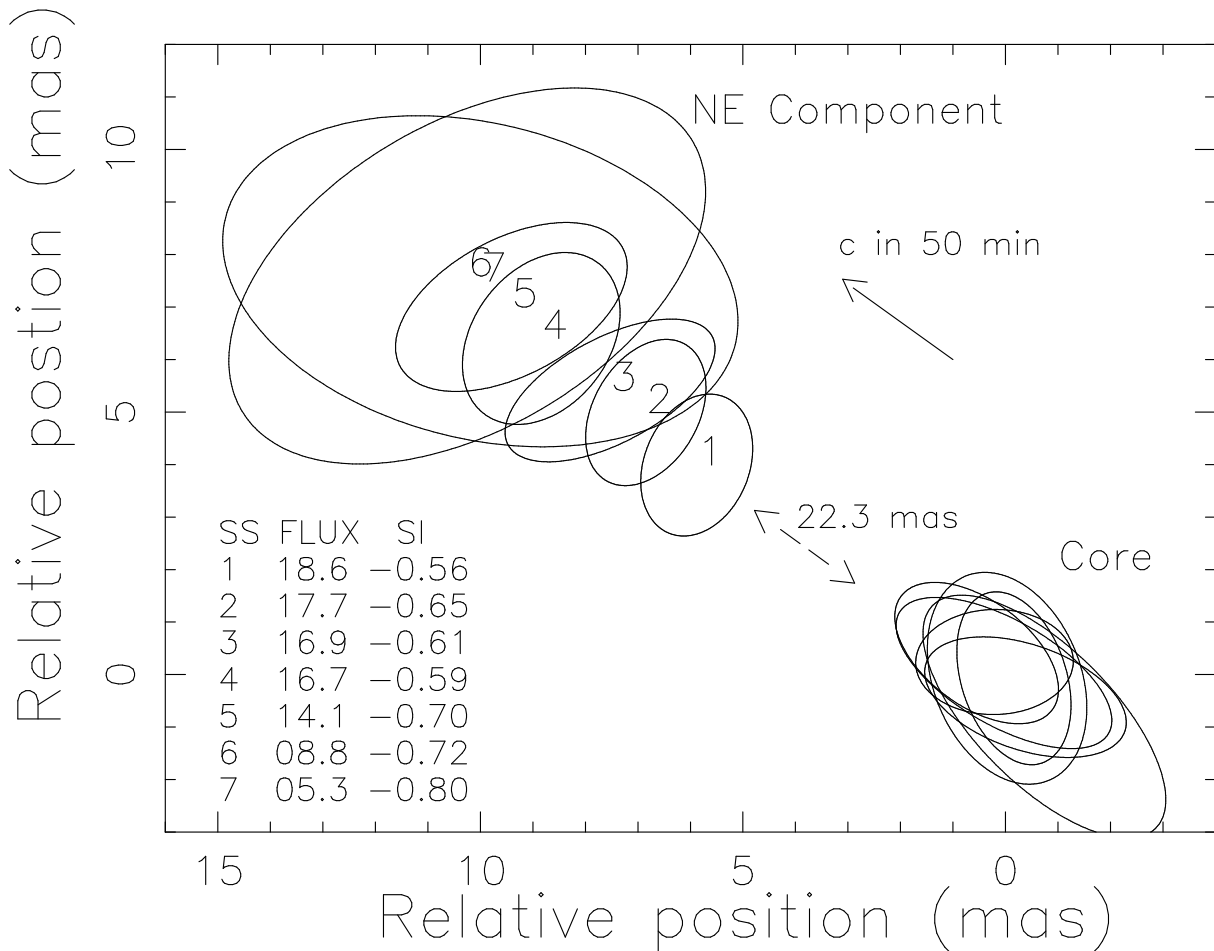


Fig. 14.— **The Expansion of the NE component on MJD 50871.** The position and full-width half-intensity angular size of the NE component and core component on MJD 50871 are shown by the ellipses. The components have been moved closer together by 22.3 mas in position angle  $54^\circ$  to fit on the plot. The numbers at the center of the NE component ellipses indicate the snapshot number (SS) which are separated in time by 50-minutes. No snapshot number is given for the core component since it is more stationary. The arrow labeled 'c in 50 min' shows the distance that a light signal will travel in the plane of the sky in 50 minutes. For each snapshot (SS), the total flux density (FLUX) and spectral index (SI) is given for the NE component.

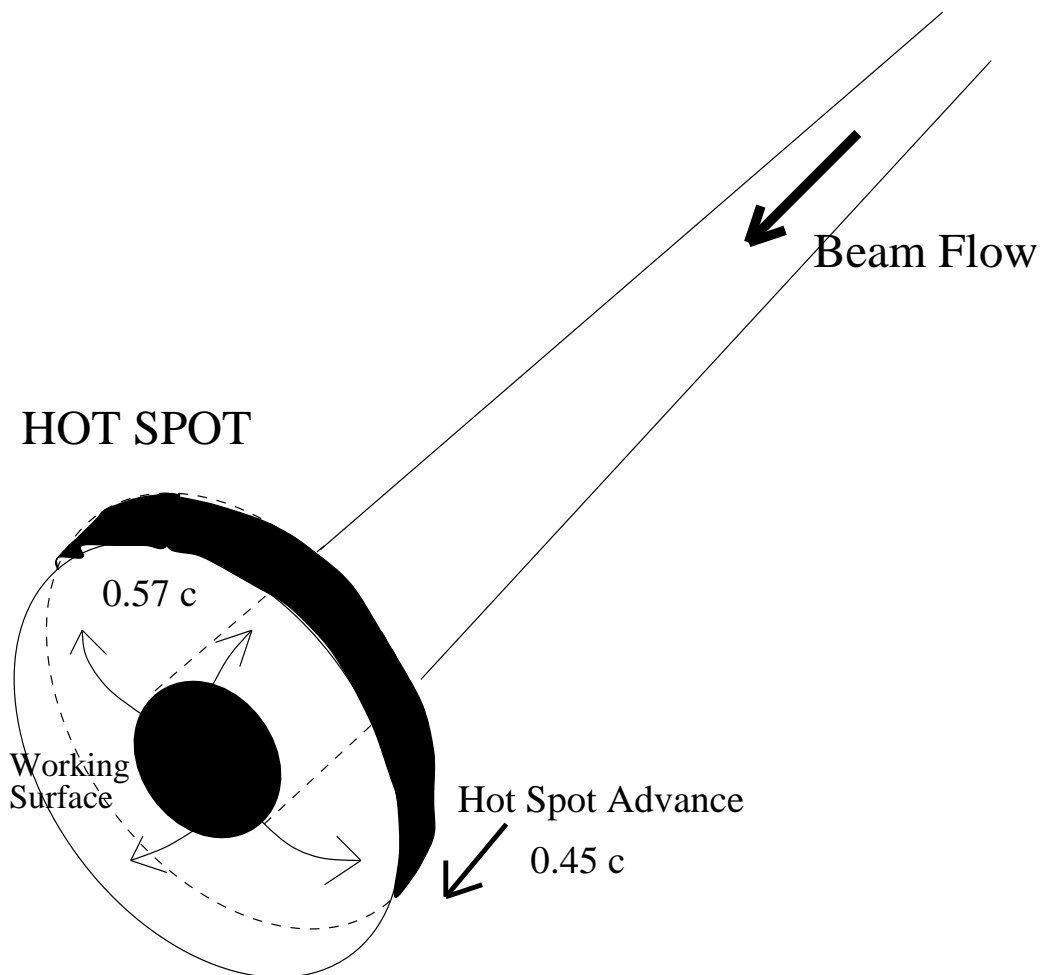


Fig. 15.— **Schematic of Lobe in Sco X-1.** A beam of energy from the binary region of Sco X-1 interacts with the ambient material to form a working surface composed of an ultra-relativistic plasma. Radiating electrons diffuse with  $v = 0.57c$  along the radial magnetic field lines to form the lobe. The working surface is also moving at  $\approx 0.45c$  at  $45^\circ$  to the line of sight. The minimum diameter of the lobe is 1.5 mas ( $3 \times 10^8$  km) and 0.6 mas ( $1.3 \times 10^8$  km) perpendicular and parallel, respectively, to the lobe motion.

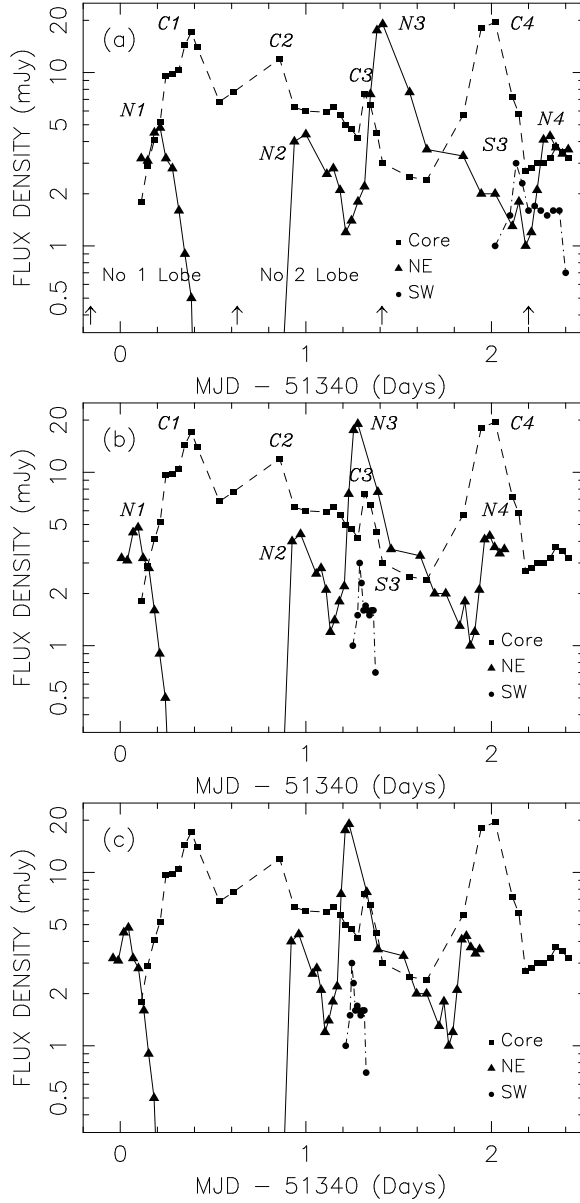


Fig. 16.— **The Correlation of Variations in the Core and Lobes in 1999 June.** (a) The observed flux densities of the core and both lobes, (b) the flux densities with the NE and SW lobes corrected for a beam speed of  $\beta_j = 1.0$  and (c) the flux densities with the NE and SW lobes corrected for a beam speed of  $\beta_j = 0.9$ . The flux density scale is logarithmic. The major lobe flares for the core are C1, C2, C3, C4; for the NE lobe are N1, N2, N3, N4; for the SW lobe, the only detected flare, is indicated by S3. The arrows on the abscissa of (a) indicated the time of minimum light for the binary system.